

## CLUSTERING OF DESI GALAXIES SPLIT BY THERMAL SUNYAEV-ZELDOVICH EFFECT

M. RASHKOVETSKYI<sup>1,2,3,4,5</sup>, D. J. EISENSTEIN<sup>1</sup>, J. AGUILAR<sup>6</sup>, S. AHLEN<sup>7</sup>, A. ANAND<sup>6</sup>, D. BIANCHI<sup>8,9</sup>,  
 D. BROOKS<sup>10</sup>, F. J. CASTANDER<sup>11,12</sup>, T. CLAYBAUGH<sup>6</sup>, A. CUCEU<sup>6</sup>, K. S. DAWSON<sup>13</sup>, A. DE LA MACORRA<sup>14</sup>,  
 ARJUN DEY<sup>15</sup>, P. DOEL<sup>10</sup>, S. FERRARO<sup>6,16</sup>, A. FONT-RIBERA<sup>17</sup>, J. E. FORERO-ROMERO<sup>18,19</sup>,  
 E. GAZTAÑAGA<sup>11,20,12</sup>, G. GUTIERREZ<sup>21</sup>, H. K. HERRERA-ALCANTAR<sup>22,23</sup>, K. HONSCHIED<sup>16,3,5</sup>, C. HOWLETT<sup>16,24</sup>,  
 M. ISHAK<sup>25</sup>, R. JOYCE<sup>15</sup>, R. KEHOE<sup>26</sup>, T. KISNER<sup>6</sup>, A. KREMIN<sup>6</sup>, O. LAHAV<sup>10</sup>, A. LAMBERT<sup>6</sup>,  
 M. LANDRIAUX<sup>6</sup>, M. MANERA<sup>27,17</sup>, R. MIQUEL<sup>28,17</sup>, E. MUELLER<sup>29</sup>, S. NADATHUR<sup>20</sup>,  
 N. PALANQUE-DELABROUILLE<sup>23,6</sup>, W. J. PERCIVAL<sup>30,31,32</sup>, F. PRADA<sup>33</sup>, I. PÉREZ-RÀFOLS<sup>34</sup>, A. J. ROSS<sup>2,4,5</sup>,  
 G. ROSSI<sup>35</sup>, E. SANCHEZ<sup>36</sup>, D. SCHLEGEL<sup>6</sup>, M. SCHUBNELL<sup>37,38</sup>, J. SILBER<sup>6</sup>, D. SPRAYBERRY<sup>15</sup>, G. TARLÉ<sup>38</sup>,  
 B. A. WEAVER<sup>15</sup>, R. ZHOU<sup>6</sup>, AND H. ZOU<sup>39</sup>

<sup>1</sup> Center for Astrophysics | Harvard & Smithsonian, 60 Garden Street, Cambridge, MA 02138, USA

<sup>2</sup> Center for Cosmology and AstroParticle Physics, The Ohio State University, 191 West Woodruff Avenue, Columbus, OH 43210, USA

<sup>3</sup> Department of Physics, The Ohio State University, 191 West Woodruff Avenue, Columbus, OH 43210, USA

<sup>4</sup> Department of Astronomy, The Ohio State University, 4055 McPherson Laboratory, 140 W 18th Avenue, Columbus, OH 43210, USA

<sup>5</sup> The Ohio State University, Columbus, 43210 OH, USA

<sup>6</sup> Lawrence Berkeley National Laboratory, 1 Cyclotron Road, Berkeley, CA 94720, USA

<sup>7</sup> Department of Physics, Boston University, 590 Commonwealth Avenue, Boston, MA 02215 USA

<sup>8</sup> Dipartimento di Fisica “Aldo Pontremoli”, Università degli Studi di Milano, Via Celoria 16, I-20133 Milano, Italy

<sup>9</sup> INAF-Osservatorio Astronomico di Brera, Via Brera 28, 20122 Milano, Italy

<sup>10</sup> Department of Physics & Astronomy, University College London, Gower Street, London, WC1E 6BT, UK

<sup>11</sup> Institut d’Estudis Espacials de Catalunya (IEEC), c/ Esteve Terradas 1, Edifici RDIT, Campus PMT-UPC, 08860 Castelldefels, Spain

<sup>12</sup> Institute of Space Sciences, ICE-CSIC, Campus UAB, Carrer de Can Magrans s/n, 08913 Bellaterra, Barcelona, Spain

<sup>13</sup> Department of Physics and Astronomy, The University of Utah, 115 South 1400 East, Salt Lake City, UT 84112, USA

<sup>14</sup> Instituto de Física, Universidad Nacional Autónoma de México, Circuito de la Investigación Científica, Ciudad Universitaria, Cd. de México C. P. 04510, México

<sup>15</sup> NSF NOIRLab, 950 N. Cherry Ave., Tucson, AZ 85719, USA

<sup>16</sup> University of California, Berkeley, 110 Sproul Hall #5800 Berkeley, CA 94720, USA

<sup>17</sup> Institut de Física d’Altes Energies (IFAE), The Barcelona Institute of Science and Technology, Edifici Cn, Campus UAB, 08193, Bellaterra (Barcelona), Spain

<sup>18</sup> Departamento de Física, Universidad de los Andes, Cra. 1 No. 18A-10, Edificio Ip, CP 111711, Bogotá, Colombia

<sup>19</sup> Observatorio Astronómico, Universidad de los Andes, Cra. 1 No. 18A-10, Edificio H, CP 111711 Bogotá, Colombia

<sup>20</sup> Institute of Cosmology and Gravitation, University of Portsmouth, Dennis Sciama Building, Portsmouth, PO1 3FX, UK

<sup>21</sup> Fermi National Accelerator Laboratory, PO Box 500, Batavia, IL 60510, USA

<sup>22</sup> Institut d’Astrophysique de Paris, 98 bis boulevard Arago, 75014 Paris, France

<sup>23</sup> IRFU, CEA, Université Paris-Saclay, F-91191 Gif-sur-Yvette, France

<sup>24</sup> School of Mathematics and Physics, University of Queensland, Brisbane, QLD 4072, Australia

<sup>25</sup> Department of Physics, The University of Texas at Dallas, 800 W. Campbell Rd., Richardson, TX 75080, USA

<sup>26</sup> Department of Physics, Southern Methodist University, 3215 Daniel Avenue, Dallas, TX 75275, USA

<sup>27</sup> Departament de Física, Serra Húnter, Universitat Autònoma de Barcelona, 08193 Bellaterra (Barcelona), Spain

<sup>28</sup> Institut Català de Recerca i Estudis Avançats, Passeig de Lluís Companys, 23, 08010 Barcelona, Spain

<sup>29</sup> Department of Physics and Astronomy, University of Sussex, Brighton BN1 9QH, U.K

<sup>30</sup> Department of Physics and Astronomy, University of Waterloo, 200 University Ave W, Waterloo, ON N2L 3G1, Canada

<sup>31</sup> Perimeter Institute for Theoretical Physics, 31 Caroline St. North, Waterloo, ON N2L 2Y5, Canada

<sup>32</sup> Waterloo Centre for Astrophysics, University of Waterloo, 200 University Ave W, Waterloo, ON N2L 3G1, Canada

<sup>33</sup> Instituto de Astrofísica de Andalucía (CSIC), Glorieta de la Astronomía, s/n, E-18008 Granada, Spain

<sup>34</sup> Departament de Física, EEBE, Universitat Politècnica de Catalunya, c/Eduard Maristany 10, 08930 Barcelona, Spain

<sup>35</sup> Department of Physics and Astronomy, Sejong University, 209 Neungdong-ro, Gwangjin-gu, Seoul 05006, Republic of Korea

<sup>36</sup> CIEMAT, Avenida Complutense 40, E-28040 Madrid, Spain

<sup>37</sup> Department of Physics, University of Michigan, 450 Church Street, Ann Arbor, MI 48109, USA

<sup>38</sup> University of Michigan, 500 S. State Street, Ann Arbor, MI 48109, USA

<sup>39</sup> National Astronomical Observatories, Chinese Academy of Sciences, A20 Datun Road, Chaoyang District, Beijing, 100101, P. R. China

Version October 23, 2025

## ABSTRACT

The thermal Sunyaev-Zeldovich (tSZ) effect is associated with galaxy clusters — extremely large and dense structures tracing the dark matter with a higher bias than isolated galaxies. We propose to use the tSZ data to separate galaxies from redshift surveys into distinct subpopulations corresponding to different densities and biases independently of the redshift survey systematics. Leveraging the information from different environments, as in density-split and density-marked clustering, is known to tighten the constraints on cosmological parameters, like  $\Omega_m$ ,  $\sigma_8$  and neutrino mass. We use data from the Dark Energy Spectroscopic Instrument (DESI) and the Atacama Cosmology Telescope (ACT) in their region of overlap to demonstrate informative tSZ splitting of Luminous Red Galaxies (LRGs). We

discover a significant increase in the large-scale clustering of DESI LRGs corresponding to detections starting from 1-2 sigma in the ACT DR6 + *Planck* tSZ Compton- $y$  map, below the cluster candidate threshold (4 sigma). We also find that such galaxies have higher line-of-sight coordinate (and velocity) dispersions and a higher number of close neighbors than both the full sample and near-zero tSZ regions. We produce simple simulations of tSZ maps that are intrinsically consistent with galaxy catalogs and do not include systematic effects, and find a similar pattern of large-scale clustering enhancement with tSZ effect significance. Moreover, we observe that this relative bias pattern remains largely unchanged with variations in the galaxy-halo connection model in our simulations. This is promising for future cosmological inference from tSZ-split clustering with semi-analytical models. Thus, we demonstrate that valuable cosmological information is present in the lower signal-to-noise regions of the thermal Sunyaev-Zeldovich map, extending far beyond the individual cluster candidates.

**Keywords:** Cosmology; Large-scale structure of the universe; Redshift surveys; Cosmic microwave background radiation; Sunyaev-Zeldovich effect; Galaxy clusters; Galaxy dark matter halos; Astronomy data analysis

## 1. INTRODUCTION

Modern cosmology is a high-precision science thanks to a rich variety of data collected. The large-scale structure of the Universe contributes a major portion of this data. Most important techniques include baryon acoustic oscillations distance measurements (e.g., DESI Collaboration et al. 2025b,a) and full-shape clustering analyses (DESI Collaboration et al. 2024a, 2025h), both based on galaxy redshift surveys.

Looking into the future, it is important to determine priorities for the next spectroscopic surveys. The expansion towards higher redshifts is well motivated by the primordial Universe studies and supported by rigorous forecasts. However, observations pose new challenges as spectral features of galaxies redshift out of the near-visible range accessible to ground-based telescopes (Ferraro et al. 2022).

In contrast, measuring more galaxy spectra at lower redshifts is easier technically. We already have a dense sample in the DESI Bright Galaxy Survey (Hahn et al. (2023)). In the future DESI upgrade, DESI-II, the density of the luminous red galaxy (LRG) sample will also increase greatly (Schlegel et al. 2022). Expansion and growth history of the Universe at low and intermediate redshifts  $z \lesssim 1$  is sensitive to the (late-time) dark energy (DESI Collaboration et al. 2025a) as well as curvature (Chen & Zaldarriaga 2025) and even early dark energy (Chaussidon et al. 2025). However, smaller available volume at lower redshifts limits the large-scale information, motivating the push towards smaller, non-linear scales, with which robust results and forecasts have been very challenging.

There are promising ideas for leveraging information from different galaxy environments that can benefit from dense samples. One is density-marked clustering, which assigns additional weight to galaxies based on a local density estimate at their location. It was originally introduced in White (2016) to enhance modified gravity tests, and was later tuned to give tighter constraints on neutrino mass (Massara et al. 2021) and other cosmological parameters (Massara et al. 2023, 2024). Analytical models of density-marked clustering were also proposed by Aviles et al. (2020); Philcox et al. (2020, 2021); Ebina & White (2025). Another is density-split clustering, which splits galaxies into subsamples based on the local den-

sity estimate. It was introduced for better modeling of redshift-space distortions in Paillas et al. (2021). Later works predict tighter constraints on standard cosmological parameters and neutrino masses (Paillas et al. 2023), or primordial non-Gaussianity (Morawetz et al. 2025). A simulation-based model of density-split clustering was built (Cuesta-Lazaro et al. 2024) and applied to BOSS CMASS data (Paillas et al. 2024), surpassing the standard analysis.

A number of works demonstrated the benefit of combining galaxy surveys with data on secondary cosmic microwave background (CMB) anisotropies, particularly lensing. For example, Farren et al. (2024); Kim et al. (2024); Sailer et al. (2025) cross-correlate lensing with photometric galaxies to better constrain the growth of cosmic structure, and Krolewski et al. (2024); Bermejo-Climent et al. (2025) improve measurements of primordial non-Gaussianity. Maus et al. (2025) present an even broader joint analysis of spectroscopic galaxy clustering and cross-correlation of photometric galaxies with CMB lensing to constrain the  $z \sim 1$  clustering amplitude and test general relativity. This combination of probes is very promising, because DESI is taking galaxy spectra at an unprecedented rate, and the next CMB experiments like Simons Observatory (Ade et al. 2019) and CMB-S4 (Abazajian et al. 2019; Carlstrom et al. 2019) have great prospects for secondary CMB anisotropies, including lensing and Sunyaev-Zeldovich effects.

We decided to use the thermal Sunyaev-Zeldovich (tSZ) effect as a means of separating galaxies into different host environments. The effect is produced by inverse Compton scattering of cosmic microwave background (CMB) photons on free thermal electrons moving randomly (whereas bulk motions give rise to the kinetic or kinematic Sunyaev-Zeldovich effect). This process results in a net increase in energy of scattered photons and creates a distinct frequency-dependent distortion in the CMB spectrum. Accordingly, CMB experiments observing in different frequency bands can disentangle tSZ emission from other components of the microwave sky. The relative change in photon energy is approximately equal to the Compton  $y$  parameter, which is proportional to the integral of free electron density  $n_e$  and temperature  $T_e$  along the path (with length element  $dr$ ; Planck Collaboration et al. 2016a; Sunyaev & Zeldovich 1972):

$$y = \int \frac{k_B T_e}{m_e c^2} n_e \sigma_T dr, \quad (1)$$

other quantities are constants: electron rest mass energy  $m_e c^2$ , Boltzmann's constant  $T_e$  and Thomson scattering cross-section  $\sigma_T$ . Accordingly, the effect is strongest in ionized, hot and dense gas in or around galaxy clusters (as suggested by Sunyaev & Zeldovich 1970, 1980). The clusters represent a distinct environment.

The tSZ data comes from CMB telescopes independent of DESI, whereas density estimates depend on the galaxy observation strategies. Using different datasets would allow us to glean complementary insights, check for systematics and potentially discover new fundamental tensions. Specific improvements could include testing the conformity of different galaxy sub-types (e.g., Patej & Eisenstein 2016), improving the redshift-space distortion modeling for full-shape clustering analyses by removing a small fraction of the strongest Fingers of God (Baleato Lizancos et al. 2025), obtaining multiple tracers with better-constrained biases for the primordial non-Gaussianity measurements (similarly to Sullivan et al. 2023) or constraining environmental effects on galaxy formation or galaxy-halo connection (e.g., Yuan et al. 2024).

We need to remark that Sunyaev-Zeldovich maps have been used for cluster studies: their detection, mass determination, and more (Planck Collaboration et al. 2016b; Hilton et al. 2021; Robertson et al. 2024; Bocquet et al. 2024; Kornoelje et al. 2025; ACT/DES/HSC Collaboration et al. 2025). But rigorously detected and confirmed cluster candidates are rare. We aim to extract more information from the lower signal-to-noise parts, which comprise a much bigger fraction of the map.

This work is not going to provide the final answers and methodology, but rather motivate further developments. It is structured as follows: Section 2 introduces the data and simulations we use, Section 3 details our processing of real data and provides its results, Section 4 describes our simulation-based toy model, compares it with data and shows new insights, Section 5 concludes with a summary and a future outlook.

## 2. DATA

### 2.1. Galaxy catalog: DESI DR1 LRG

The Dark Energy Spectroscopic Instrument (DESI DESI Collaboration et al. 2016b, 2022) is a robotic fiber spectrograph operating on the 4-meter Mayall telescope at Kitt Peak National Observatory. Since 2021, it conducts an 8-year galaxy survey of approximately 40% of the sky, which will yield nearly 63 million galaxy and quasar redshifts (compared to the original forecast of 39 million for the 5-year program in Levi et al. 2013; DESI Collaboration et al. 2016a). This efficiency is enabled by instrumentation and software innovations, including a focal plane design with the robotic positioners for approximately 5000 optical fibers (Silber et al. 2023; Poppet et al. 2024), an optical corrector widening the field of view to  $\sim 3^\circ$ , a comprehensive spectroscopic reduction pipeline (Guy et al. 2023) and a pipeline to adjust observation planning and optimization as the survey progresses (Schlafly et al. 2023).

DESI's scientific program has been successfully validated (DESI Collaboration et al. 2024b) alongside the Early Data Release (DESI Collaboration et al. 2024c). The key results based on Data Release 1 (DESI Collabo-

ration et al. 2025c) include clustering catalogs and two-point statistics measurements (DESI Collaboration et al. 2025g), baryon acoustic oscillation (BAO) distance measurements from galaxies, quasars (DESI Collaboration et al. 2025f) and Lyman- $\alpha$  forest (DESI Collaboration et al. 2025d) along with their detailed implications for cosmological models (DESI Collaboration et al. 2025e); and full-shape clustering of galaxies and quasars (DESI Collaboration et al. 2024a) with their cosmological analysis (DESI Collaboration et al. 2025h). Furthermore, updated BAO measurements from Lyman- $\alpha$  (DESI Collaboration et al. 2025b), galaxies and quasars with accompanying cosmological interpretations (DESI Collaboration et al. 2025a) are also available, based on Data Release 2 (DESI Collaboration 2026).

We use Luminous Red Galaxies (LRG; Zhou et al. 2023a) from the DESI DR1 clustering catalog covering 5,740 deg<sup>2</sup> (DESI Collaboration et al. 2025g). We chose LRG because their redshift range ( $0.4 < z < 1.1$ ) covers the peak in redshift distribution of Sunyaev-Zeldovich clusters (ACT/DES/HSC Collaboration et al. 2025). We discard galaxies at  $z > 0.85$  because then both the LRG density (DESI Collaboration et al. 2025g) and the SZ cluster abundance (ACT/DES/HSC Collaboration et al. 2025) drop.

### 2.2. Sunyaev-Zeldovich map: ACT DR6

The Atacama Cosmology Telescope (ACT; Fowler et al. 2007; Choi et al. 2020) was a ground-based cosmic microwave background (CMB) experiment. Compared to the space-based *Planck* mission (Planck Collaboration et al. 2020a), it has higher resolution and lower instrumental noise, but a smaller sky fraction and fewer frequency bands (which makes component separation harder). ACT's advantages enable smaller-scale Sunyaev-Zeldovich measurements, which can be combined with robust larger-scale results from *Planck*.

We use the thermal Sunyaev-Zeldovich Compton  $y$  parameter map from ACT Data Release 6 covering  $\approx 13,000$  deg<sup>2</sup> (Coulton et al. 2024), which builds upon *Planck* data (Planck Collaboration et al. 2016a). We rely on the accompanying noise simulations (Atkins et al. 2023) to estimate the signal-to-noise ratio in our analysis. We primarily work in the  $\approx 3,510$  deg<sup>2</sup> area of overlap between DESI DR1 LRG and ACT DR6 footprints.

### 2.3. Simulations: ABACUSSUMMIT halo catalogs and ABACUSHOD galaxy-halo connection model

We also use a  $z = 0.8$  snapshot of a  $(2h^{-1}\text{Gpc})^3$  cubic box (for the fiducial cosmology) from the ABACUSSUMMIT suite of  $N$ -body simulations (Maksimova et al. 2021) produced with ABACUS code (Garrison et al. 2021). The halos have been identified with the COMPASO halo finder (Hadzhiyska et al. 2022). We use a galaxy catalog produced within the halo occupation distribution (HOD) galaxy-halo connection framework, efficiently implemented in ABACUSHOD (Yuan et al. 2022) with parameters based on Yuan et al. (2024) ( $\text{Zheng07} + f_{\text{ic}} + \alpha_c + \alpha_s$  model, but with  $f_{\text{ic}} = 1$ ). This galaxy catalog was one of the base cubic boxes for *Abacus-2* cut-sky mocks described in DESI Collaboration et al. (2025f).

## 3. MEASUREMENTS

### 3.1. Methodology and challenges

We divide the LRGs into subsamples (“SNR bins”) according to the signal-to-noise ratio at their location in the ACT DR6 + *Planck* Compton- $y$  map (Coulton et al. 2024). First, we match the positions of the LRGs from the DESI clustering catalog to the pixels in the map<sup>1</sup>. We only use the pixels with the apodized mask value above the threshold of 0.9 (this slightly reduces the footprint from  $\approx 3,510$  deg $^2$  to  $\approx 3,420$  deg $^2$ ). Second, we compute the pixel-level standard deviations in  $y$  using the corresponding 304 Gaussian noise simulation (Atkins et al. 2023). Finally, we compute the signal-to-noise ratio in each pixel by dividing the  $y$  value by its standard deviation.

Such external selection of galaxies imposes complex geometry changes that affect the estimation of the clustering statistics. E.g., the Landy-Szalay estimator (Landy & Szalay 1993) for the correlation function between samples 1 and 2 (which may be identical or different):

$$\xi_{12}^{\text{LS}} = \frac{D_1 D_2 - D_1 R_2 - R_1 D_2}{R_1 R_2} + 1, \quad (2)$$

where  $D_1 D_2$  are the (binned) pair counts between data (galaxies) from sample 1 and data 2,  $D_1 R_2$  are the pair counts between data 1 and random points (reflecting the survey geometry and selection etc) for sample 2,  $R_1 D_2$  are between random points 1 and data 2, and  $R_1 R_2$  are between random points 1 and 2.

The key to the problem is that the full-survey random catalogs are not representative of our subsamples. One might think that imposing the same on-sky position filter on random points would be a solution; however, it is not perfect. The resulting randoms would live in (narrow) “cylinders” extended along the line of sight, whereas a significant portion of selected galaxies would be truly clumped around the cluster position in a three-dimensional sense.

It is possible to accept the unusual-looking clustering measurement and model it consistently, but we have decided to keep the correlation functions more intuitive. To achieve this, we avoid the issue with the subsample geometry by employing an asymmetric Davis-Peebles estimator (Davis & Peebles 1983) for the correlation function:

$$\hat{\xi}_{12}^{\text{DP}} = \frac{D_1 D_2}{D_1 R_2} - 1. \quad (3)$$

The  $D_1 D_2$  and  $D_1 R_2$  are the same pair counts as in the Landy-Szalay estimator (Eq. (2)). However, we note that the randoms representing sample 1 are not required: neither  $R_1 D_2$  nor  $R_1 R_2$  are involved. The randoms are only necessary for sample 2. Therefore, with this estimator, we can compute the correlation function between the tSZ subsample (as 1) and the full LRG sample (as 2).

We also apply filters to the Compton- $y$  map for two reasons. First, a filter matched to a cluster SZ profile would optimally detect them and recover their positions (Turin 1960). Second, the environmental influence of a cluster is likely to extend further than its Compton parameter profile. Our fiducial filter is not thoroughly matched, but has a Gaussian shape with a 2.4

<sup>1</sup> The ACT DR6 map is provided as a rectangular grid in DEC and RA with a pixel side of 0.5 arcmin.

SNR bin	$N_{\text{LRG}}$
$(-\infty, -2) \sigma$	25101
$[-2, -1) \sigma$	130331
$[-1, 0) \sigma$	308498
$[0, 1) \sigma$	305819
$[1, 2) \sigma$	127875
$[2, 3) \sigma$	25469
$[3, 4) \sigma$	3577
$[4, 5) \sigma$	981
$[5, 6) \sigma$	484
$[6, \infty) \sigma$	676
Total	928811

**Table 1**  
Number of DESI DR1 LRGs ( $0.4 < z < 0.85$  and in the overlap with ACT footprint) in different tSZ SNR bins (after applying our fiducial Gaussian filter to the Compton- $y$  map).

arcmin full width at the half-maximum (corresponding to  $\approx 1.1 h^{-1}\text{Mpc}$  at  $z = 0.6$ ) for simplicity. The single reference filter in the ACT DR6 SZ cluster paper has the same scale (ACT/DES/HSC Collaboration et al. 2025). We apply the filter by transforming the map to spherical harmonics  $a_{lm}$ , multiplying them by the Gaussian filter profile  $f_l$ , and transforming back to the sky positions. We apply the same filter to all the noise simulations to obtain the corresponding pixel-wise standard deviation map. For reference, we provide galaxy counts in each signal-to-noise ratio bin after filtering in Table 1.

We should remark on the large areas with negative Compton  $y$  parameter, contradicting its theoretical definition (Eq. (1)). Instrumental (or atmospheric) noise plays a certain part. Kinematic Sunyaev-Zeldovich effect, resulting from the bulk motions of free electrons, can have different signs and can become partially confused with “negative” thermal effect. It is important to note that these factors produce chance fluctuations and not systematic biases, provided that the instrument bandpasses are modeled accurately. Other components, like the cosmic infrared background (CIB), may also leak into the thermal Sunyaev-Zeldovich reconstruction, potentially biasing the tSZ measurements (e.g., Liu et al. 2025a). CIB-deprojected maps are available for ACT DR6 (Coulton et al. 2024), but in multiple variants with different parameters, so we defer the consistency check with them to future work.

Finally, we briefly comment on our choice of tSZ signal-to-noise ratio ( $y/\sigma_y$ ) instead of the signal (Compton- $y$ ). The signal can be more directly related to the mass of the cluster or the dark matter halo in which the galaxy resides<sup>2</sup>. However, we want to study the low signal-to-noise regime, in which a measured Compton- $y$  inevitably corresponds to a relatively wide range of true Compton- $y$  parameters. Signal-to-noise ratio better characterizes the fraction of near-zero signal objects shifted up (or down) by noise, and we find it a more significant advantage. Moreover, the range of pixel-wise standard deviations of the Compton- $y$  parameter within the footprint (shown in Fig. 1) is quite narrow. Accordingly, we find very little difference between comparable bins in SNR ( $y/\sigma_y$ ) and

<sup>2</sup> But note that our simple filter does not exactly match the filters used in tSZ cluster studies like Hilton et al. (2021); Robertson et al. (2024); Kornoelje et al. (2025); ACT/DES/HSC Collaboration et al. (2025), so the relations calibrated there do not directly apply to our measurements.

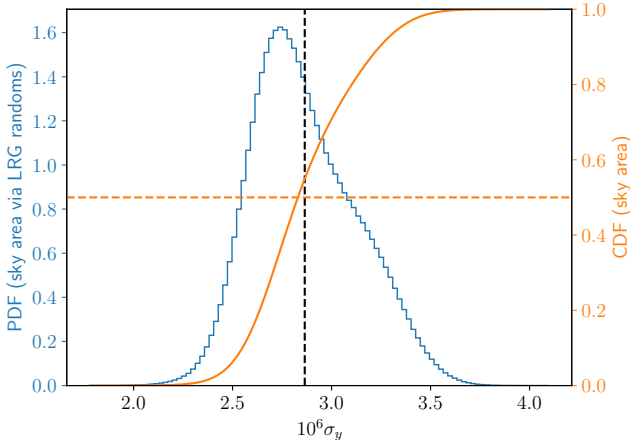


**Figure 1.** Distribution of  $\sigma_y$ , the pixel standard deviation of Compton- $y$  parameter after our filtering (over the area of the overlap of ACT DR6 and DESI DR1 footprints). The black dashed vertical line shows the mean  $\sigma_y$ . The orange dashed horizontal line denotes  $\text{CDF} = 0.5$ .

signal (Compton- $y$ ).

### 3.2. Larger-scale clustering and galaxy bias

First, we compute the larger-scale cross-correlation functions between the different SNR bins and the full LRG sample. We use the radial ( $s$ ) and angular ( $\mu$ ) binning. We disregard the pairs located too closely on the sky<sup>3</sup> for three reasons. The first is to focus on the larger-scale, 2-halo clustering (we study the 1-halo regime in Section 3.3). The second is to avoid using pairs of galaxies belonging to the same SZ pixel, or associated with the same line of sight smeared by the beam and the filter. This may also reduce sensitivity to cosmic infrared background contamination (found significant in cluster profiles at smaller radii in Liu et al. 2025a). The third is to mitigate the DESI fiber assignment incompleteness effects (DESI Collaboration et al. 2025g; Bianchi et al. 2025), for which Pinon et al. (2025) recommended the lower threshold of 0.05 degrees. We only count pairs with the angular separation above 0.1 degrees (6 arcmin)<sup>4</sup>, which corresponds to the perpendicular separation  $r_p \approx 2.7 h^{-1}\text{Mpc}$  at  $z = 0.6$ <sup>5</sup>.

We show the resulting isotropic cross-correlation functions in Fig. 2 with covariances estimated using the jackknife technique. We see a significant clustering enhancement in the monopole as the tSZ detection level increases, even though we stop at  $4\sigma$ , which was the threshold for cluster candidates in ACT/DES/HSC Collaboration et al. (2025)<sup>6</sup>. This almost certainly corresponds to an

<sup>3</sup> This is technically known as the theta ( $\theta$ ) cut. Note that here  $\theta$  is the angle between the lines of sight from the Solar System to the two galaxies, and not the angle  $\Theta$  between the line of sight and the vector from one galaxy to the other used for the binning of the correlation function in  $\mu \equiv \cos \Theta$ .

<sup>4</sup> This leaves  $\mu \approx 1$  bins with no pair counts and undefined correlation functions. We discard these bins and average over the remaining bins to obtain the correlation function monopole.

<sup>5</sup> Ranging between  $r_p \approx 1.9 h^{-1}\text{Mpc}$  at  $z = 0.4$  and  $r_p \approx 3.5 h^{-1}\text{Mpc}$  at  $z = 0.85$

<sup>6</sup> However, bear in mind the simplicity of our filter, the matched filters of ACT/DES/HSC Collaboration et al. (2025) should be more optimal.

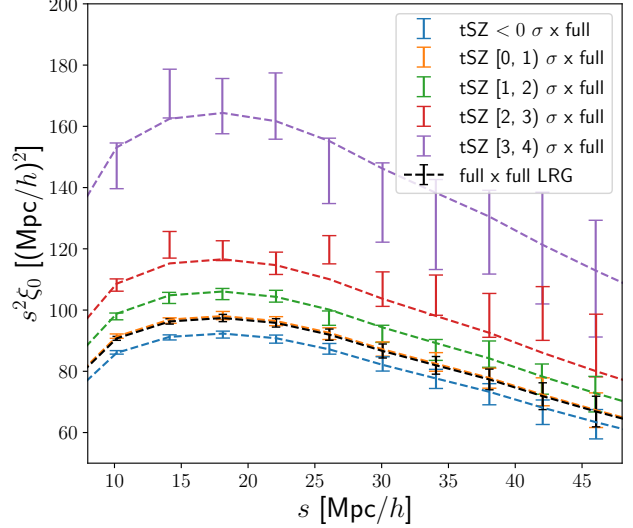


**Figure 2.** Large-scale isotropic (monopole) cross-correlation functions of different SNR bins with the full LRG sample (excluding pairs with angular separation below 0.1 degrees). (In this and the following figures, we apply our fiducial Gaussian filter to the tSZ Compton- $y$  parameter map, and use the jackknife technique to estimate errorbars.) There is a significant clustering enhancement with increasing tSZ detection level even below the threshold for cluster candidates ( $4\sigma$  in ACT/DES/HSC Collaboration et al. 2025). Colored dashed lines show the best fits obtained by scaling the full-sample autocorrelation function (black dashed line). The scaling coefficients are the relative biases shown in Fig. 3.

increase in galaxy bias.

The 0 to 1  $\sigma$  subsample appears very similar to the full LRG sample. This is not explained by the vast majority of galaxies belonging to that bin, as Fig. 1 shows it contains just  $\approx 1/3$  of our LRGs. Instead, the galaxies with negative signal and higher SNR compensate each other so that their environmental characteristics average close to this [0, 1)  $\sigma$  bin. Interestingly, this similarity holds in all other aspects we consider in this paper.

For clarity, we seek to summarize each line in Fig. 2 with a single number. A simple way is to find the scaling for the full LRG correlation function to best match the cross-correlation function with any given signal-to-noise bin. This multiplier should be similar to the ratio of the linear galaxy biases between the SNR subsample and the full LRG sample. Accordingly, we also refer to this scaling as relative galaxy bias.

The jackknife covariance estimates for each correlation function allow us to estimate the precision of the scaling. However, we have not estimated the covariances between different cross-correlation functions shown in Fig. 2 consistently. This makes our relative bias errorbar estimates imperfect and approximate.

We show the resulting galaxy biases of our subsamples (relative to the full LRG sample) in Fig. 3. The picture is consistent with the conclusions we have drawn from Fig. 2: the increase of galaxy bias with the tSZ detection level, and the 0 to 1  $\sigma$  bin being close to average over all LRGs. In addition, we can inspect more categories at negative signal-to-noise, different from the full LRG but not so significantly deviating from each other.

We also show the projected cross-correlation functions  $w_p(r_p)$  in Fig. 4. We have computed it with the

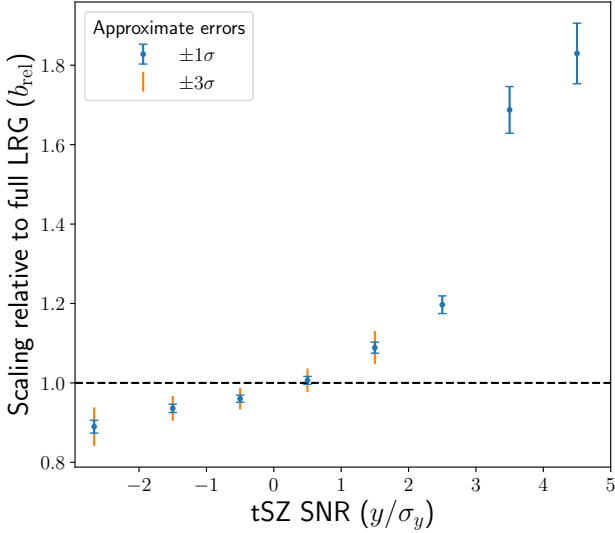


**Figure 3.** Galaxy bias of different SNR bins relative to the full LRG sample. These numbers are based on the ratio of the corresponding correlation functions from Fig. 2. The bias increase (clustering enhancement) can be seen more concisely here. For smaller errorbars, which can not be seen well, we also show 3 $\sigma$  bars (exactly 3 times larger).

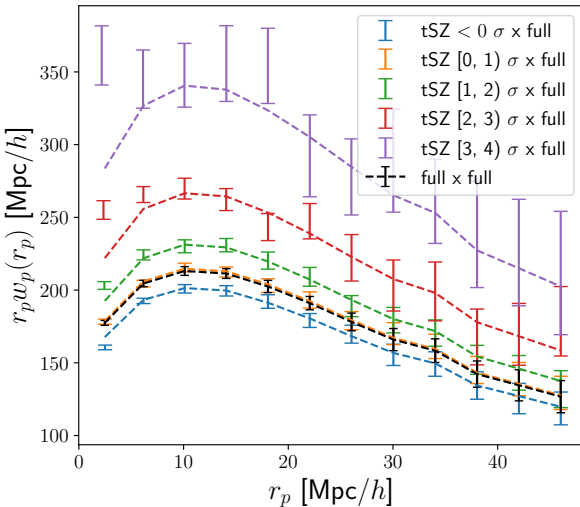


**Figure 4.** Projected cross-correlation functions of different SNR bins with the full LRG sample. The line-of-sight separation limit is  $\pi_{\max} = 50 h^{-1} \text{Mpc}$  (and we do not exclude pairs with small angular separations). Colored dashed lines show the best fits (using  $r_p > 8 h^{-1} \text{Mpc}$ ) obtained by scaling the full-sample auto-correlation function (black dashed line). The clustering enhancement is notable, as with the correlation function monopole (Fig. 2). The relative biases obtained from projected clustering are consistent with Fig. 3, but have larger errorbars.

line-of-sight separation upper limit  $\pi_{\max} = 50 h^{-1} \text{Mpc}$  and without excluding pairs with small angular separation. The cross-correlation functions still resemble the scaled full-sample auto-correlation on larger scales ( $r_p \gtrsim 8 h^{-1} \text{Mpc}$ ). The resulting relative bias values are close to our results from the 3D monopoles (Fig. 3). This means that the pattern of stronger clustering with higher tSZ SNR is consistent between the two statistics.

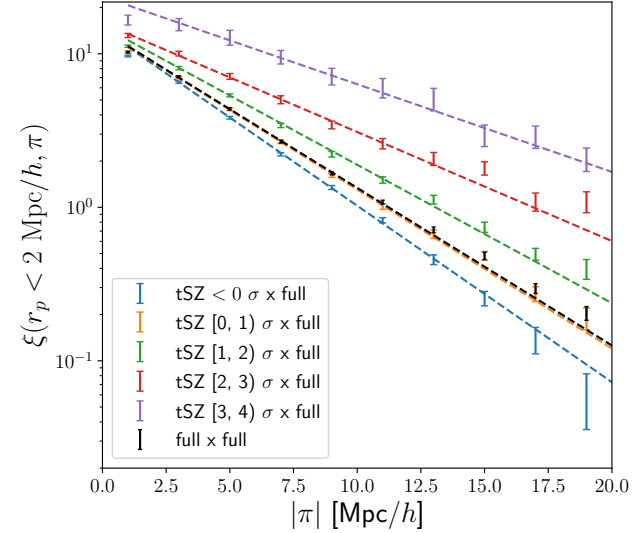


**Figure 5.** Small-scale line-of-sight cross-correlation functions of different SNR bins with the full LRG sample (not excluding pairs with small angular separations). The dashed lines show the best-fit exponentials according to Eq. (4). There is not only an increase in amplitude, but also a flattening of the slopes of the curves with increasing tSZ SNR, indicating regions with higher tSZ signal have hotter small-scale velocity dispersions.

The projected correlation function is beneficial because it marginalizes over redshift-space distortions, simplifying the modeling and interpretation. On the flip side, we obtain slightly larger errorbars on relative bias obtained from projected clustering, but this depends on the ranges, which we have not optimized thoroughly in this proof-of-concept work. In addition, precise redshifts are not critical for projected statistics. This can allow future usage of a larger “extended” photometric LRG sample from DESI Legacy Surveys imaging (Zhou et al. 2023b), which also has more overlap area with ACT.

### 3.3. Small-scale line-of-sight clustering and velocity dispersions

The cluster (supercluster) peculiar velocities are most apparent in configuration space at small scales near the line of sight. Here we switch the correlation function bins from  $s$  and  $\mu$  to the line-of-sight ( $\pi$ ) and the perpendicular (on-sky,  $r_p$ ) separations between the galaxy pair members. In this section, we also do not discard pairs with small angular separations, so the resulting clustering measurements are likely affected by DESI fiber assignment incompleteness (DESI Collaboration et al. 2025; Bianchi et al. 2025; Pinon et al. 2025).

Accordingly, we plot the line-of-sight small-scale correlation functions for our SNR bins in Fig. 5. We notice an increase in correlation functions with the tSZ detection level in each bin, similar to the trends in larger-scale correlation functions (Fig. 2). More interestingly, the slopes of the curves are also noticeably different, although it is hard to judge the significance of these differences visually.

To better quantify the slopes, we fit exponentials to the correlation functions:

$$\xi(\pi) \approx C \exp\left(-\sqrt{2} \frac{|\pi|}{\sigma_\pi}\right). \quad (4)$$

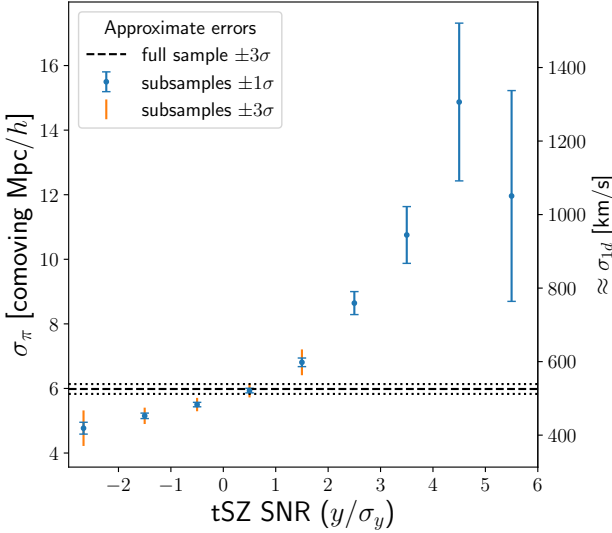


**Figure 6.** One-dimensional comoving coordinate dispersions  $\sigma_\pi$  from small-scale line-of-sight clustering (Fig. 5) via Eq. (4). Approximate conversion to one-dimensional (line-of-sight) velocity dispersions  $\sigma_{1d}$  via Eq. (6) is provided on the right. The dispersion values increase with the signal-to-noise ratio, except the 5 to 6  $\sigma_y$  bin. For smaller errorbars, which can not be seen well, we also show  $3\sigma$  bars (exactly 3 times larger).

$\sigma_\pi$  gives the one-dimensional dispersion (standard deviation). This is motivated by the exponential fit to the distributions of peculiar radial velocities (Peebles 1976) and a physical Press–Schechter (Gaussian mixture) model (Sheth 1996). The peculiar radial velocity  $v_\parallel$  is related to the line-of-sight displacement between real and redshift space  $\Delta\pi$  via (Kaiser 1987; Chen et al. 2025)

$$\Delta\pi = \frac{1+z}{H(z)} v_\parallel. \quad (5)$$

Because we have a wide redshift range ( $z = 0.4 – 0.85$ ), we can not use this equation for exact conversion. However, we obtain approximate velocity dispersion figures by substituting the middle redshift  $z_{\text{mid}} = 0.625$ :

$$\sigma_{1d} \approx \frac{H(z_{\text{mid}})}{1+z_{\text{mid}}} \sigma_\pi. \quad (6)$$

We plot the results of fitting Eq. (4) for each tSZ SNR bin in Fig. 6. We measure them in comoving line-of-sight separations, but also provide an approximate conversion to line-of-sight peculiar velocities using the average redshift. The dispersions increase with the tSZ detection level, more significantly for positive values<sup>7</sup>.

The increases in velocity dispersion (Fig. 6) and galaxy bias (Fig. 3) should be related. Assuming the relation between halo mass and tSZ observables, they are two differently weighted integrals over the halo mass function. Consistency of these patterns could be a powerful test of the  $M_{\text{halo}} – y$  relation, or systematics, but the DESI fiber assignment (Bianchi et al. 2025) brings further complications.

The 0 to 1  $\sigma_y$  bin is again very close to the full LRG sample. This is interesting because the full sample

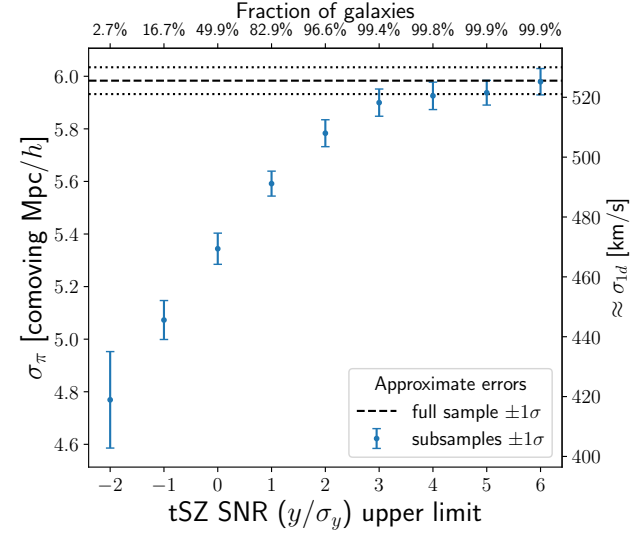


**Figure 7.** One-dimensional comoving coordinate dispersions  $\sigma_\pi$  from small-scale line-of-sight clustering for subsamples strictly below a given tSZ SNR (“cumulative bins”) obtained by fitting Eq. (4). Approximate conversion to one-dimensional (line-of-sight) velocity dispersions  $\sigma_{1d}$  via Eq. (6) is provided on the right. On top, we list fractions of the full sample belonging to each subsample.

presumably includes very large clusters with extremely strong Fingers of God, unlike the  $[0, 1)$  SNR bin. However, the large cluster contribution should be suppressed by the DESI fiber assignment incompleteness (Bianchi et al. 2025), which could partially explain the similarity.

Following Baleato Lizancos et al. (2025), we also consider the lessening of Fingers of God by putting an upper limit on galaxies’ tSZ SNR. We construct subsamples strictly below several tSZ SNR values (“cumulative bins”), compute their line-of-sight clustering and extract coordinate dispersions  $\sigma_\pi$ . We show the results in Fig. 7. It shows that the velocity dispersion could be lowered by  $\approx 20\%$  (at tSZ SNR  $< -2$ ), but at the cost of discarding  $\approx 97\%$  of galaxies. The optimal cutoff is probably closer to an SNR of 1 or 2.

Another natural way to summarize Fig. 5 would be by integrating the correlation functions. This is directly related to the average number of any LRGs in narrow cylinders with axes along the line of sight centered on LRGs belonging to a particular SNR bin. We provide this summary in Fig. 8. The average number of neighbors increases, in accordance with the expectation that LRGs with higher tSZ SNR tend to live in larger clusters.

We have found even more striking differences in the abundance of galaxies with many neighbors in different SNR bins. However, it is hard to visualize and interpret more meaningfully.

#### 4. SIMULATION-BASED TOY MODEL

We aim to simulate both galaxy catalogs and the Compton- $y$  map consistently. Galaxy catalogs are often made from  $N$ -body simulations using a halo occupation distribution (HOD). The process has been highly optimized in ABACUSHOD (Yuan et al. 2022). Therefore, we choose to make a Compton parameter map from a halo catalog.

Our general strategy is to reproduce our analysis of the data with some simplification. We make pixelated

<sup>7</sup> The last, 5 to 6  $\sigma_y$  bin, is an exception, although it has a large errorbar

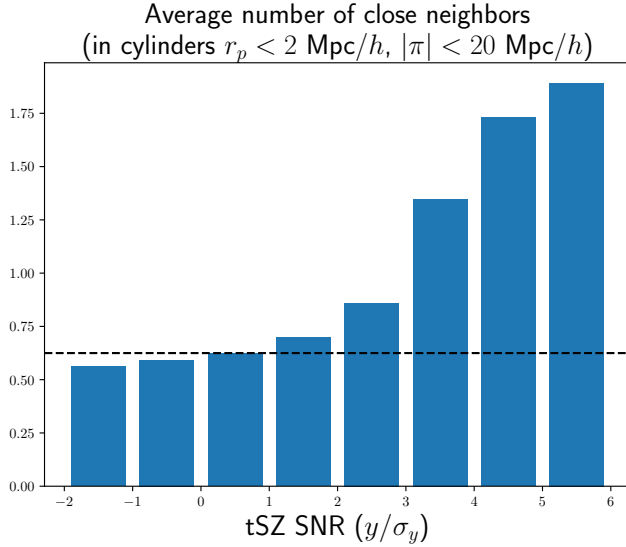


**Figure 8.** Average number of close neighbors in different tSZ SNR bins. (No lower limit on angular separation is applied.) It increases, confirming that stronger tSZ signatures are associated with clusters that have more galaxies. The dashed horizontal line shows the full-sample average number of neighbors, which is again very close to the  $[0, 1) \sigma$  subsample.

square maps from a halo catalog in a cubic periodic box using a flat-sky approximation. We make these maps for mock Compton- $y$  measurements (true signal plus noise) and their pixel-wise standard deviation  $\sigma_y$  (mimicking patterns from the overlap of ACT and DESI footprints). We then take an HOD mock galaxy catalog produced from the same halo catalog, find the pixel corresponding to each galaxy position, and take the galaxy’s tSZ SNR from that pixel. Finally, we separate the mock galaxies into categories (bins) by this property and compute cross-correlation functions between these categories and the full set of mock galaxies.

We are aware of the advanced models for SZ-halo connection informed by hydrodynamic simulations or observations (e.g., Stein et al. 2020; Osato & Nagai 2023; Liu et al. 2025b). However, in this proof-of-concept work, we choose to develop a simpler model that is easier to control.

#### 4.1. Simple $y$ signal map from an $N$ -body simulation

The Compton  $y$  parameter depends on the electron temperature  $T_e(\mathbf{r})$  and number density  $n_e(\mathbf{r})$  as functions of spatial position  $\mathbf{r}$ , whereas an  $N$ -body simulation provides masses and positions of discrete dark matter particles grouped in halos. Let us recall the theoretical expression for  $y$  as the integral along the line of sight (Planck Collaboration et al. 2016a; Sunyaev & Zeldovich 1972):

$$y(\boldsymbol{\theta}) = \int_0^{r_{ls}} \frac{k_B T_e(r, \boldsymbol{\theta})}{m_e c^2} n_e(r, \boldsymbol{\theta}) \sigma_T dr. \quad (7)$$

The integral above is taken along the radial coordinate  $r$  to the last scattering surface  $r_{ls}$ , where CMB emerges.  $k_B$  is the Boltzmann’s constant,  $m_e c^2$  is the electron’s rest energy and  $\sigma_T$  is the Thomson cross-section.

We estimate electron temperatures  $T_e$  using the motions of dark matter particles in halos. The root-mean-

square thermal velocity is analogous to the random velocity dispersion of particles. The velocity dispersion of dark matter particles belonging to each halo is available in the ABACUSSUMMIT COMPASO halo catalogs (Hadzhiyska et al. 2022). The remaining non-trivial step is connecting dark matter to hot gas. We assume complete ionization, primordial composition<sup>8</sup>, and thermal equilibrium between ions and electrons in the gas. We find adequate hot gas temperatures<sup>9</sup> by taking the same kinetic energy of random motions per unit mass as for dark matter particles (similarly to Diaferio et al. 2000):

$$\frac{1}{2} \mu m_p \sigma_{3d}^2 \approx \frac{3}{2} k_B T_e. \quad (8)$$

$\sigma_{3d}$  is the 3D velocity dispersion of dark matter particles within the halo,  $k_B$  is Boltzmann’s constant, and  $\mu$  is the mean mass per particle in units of proton mass  $m_p$ , neglecting the electron mass:

$$\mu \approx \left( 2 - \frac{5}{4} Y_{\text{He}} \right)^{-1}, \quad (9)$$

where  $Y_{\text{He}}$  is the mass fraction of helium.

Then, we approximately compute the number of electrons  $N_e$  from the dark matter mass. First, we obtain the baryonic matter mass using the global baryon-to-dark matter ratio given by the cosmic density parameters  $\Omega_b/\Omega_{\text{cdm}}$  (Diaferio et al. 2000). Second, we estimate the hot gas mass by assuming it constitutes a constant fraction of all baryons  $f_{\text{hot}} \approx 0.85$  (Fukugita et al. 1998). Either of these coefficients may be imprecise, but this can be corrected for in the scaling calibration we perform in Section 4.3. Finally, we compute the electron number  $N_e$  assuming complete ionization of the hot gas and primordial composition as previously:

$$N_e \approx \left( 1 - \frac{1}{2} Y_{\text{He}} \right) f_{\text{hot}} \frac{\Omega_b}{\Omega_{\text{cdm}}} \frac{M_{\text{halo}}}{m_p}. \quad (10)$$

We could also have arrived at the same scaling between the number density of electrons  $n_e$  and the mass density of dark matter:

$$n_e \approx \left( 1 - \frac{1}{2} Y_{\text{He}} \right) f_{\text{hot}} \frac{\Omega_b}{\Omega_{\text{cdm}}} \frac{\rho_{\text{dm}}}{m_p}, \quad (11)$$

but scaling between densities is a stronger assumption than scaling between the total mass and number of electrons. Moreover, we do not use the detailed density profiles for our final mock maps.

Using Eqs. (7), (8) and (11), we can arrive at a simple expectation for (central) Compton- $y$  parameter from a halo. First, we obtain  $y \propto \sigma_{3d}^2 \int \rho_{\text{dm}} dl$ . Then, we can estimate  $\int \rho_{\text{dm}} dl \propto M_{\text{halo}}/R_{\text{halo}}^2$ . A simplistic definition of a halo is a spherical region with a fixed high density<sup>10</sup>, so  $M_{\text{halo}} \propto R_{\text{halo}}^3$ . Assuming virialization,  $\sigma_{3d}^2 \propto M_{\text{halo}}/R_{\text{halo}}$ . Putting all together gives  $y \propto M_{\text{halo}}$ , although halos can violate the underlying assumptions (and we see a steeper relation in Section 4.6 and Fig. 12).

<sup>8</sup> I.e., mix of hydrogen-1 and helium-4 with the mass fraction of the latter  $Y_{\text{He}} = 0.2454$  (Planck Collaboration et al. 2020b).

<sup>9</sup> The 3-dimensional velocity dispersion  $\sigma_{3d} \sim 200 \text{ km s}^{-1}$  yields  $T_e \sim 10^6 \text{ K}$ .

<sup>10</sup> However, constant density does not hold in modern halo finders, including COMPASO (Hadzhiyska et al. 2022).

To proceed further, we use the simplifying flat-sky approximation valid for small angular scales for simplicity. Accordingly, we switch from  $\mathbf{r} = (r, \theta)$  decomposition to  $(r_{\parallel}, \mathbf{r}_{\perp})$ :

$$y(\mathbf{r}_{\perp}) \approx \frac{k_B \sigma_T}{m_e c^2} \int_0^{r_{\max}} T_e(r_{\parallel}, \mathbf{r}_{\perp}) n_e(r_{\parallel}, \mathbf{r}_{\perp}) dr_{\parallel}. \quad (12)$$

Next, we need to account for particle discreteness. As the first rough approximation, we take infinitely narrow profiles of  $T_e(\mathbf{r}) n_e(\mathbf{r})$  for each dark matter particle with the 3-dimensional Dirac delta function  $\delta^{(3)}$ :

$$y(\mathbf{r}_{\perp}) \approx \frac{k_B \sigma_T}{m_e c^2} \sum_j \int_0^{r_{\max}} T_{e,j} N_{e,j} \delta^{(3)}(\mathbf{r} - \mathbf{r}_j) dr_{\parallel}. \quad (13)$$

Here  $j$  indexes dark matter particles with positions  $\mathbf{r}_j$  and the corresponding electron temperature and number estimates. We can evaluate the integral over  $r_{\parallel}$  by decomposing the delta function in  $r_{\parallel}$  and  $r_{\perp}$ <sup>11</sup>:

$$y(\mathbf{r}_{\perp}) \approx \frac{k_B \sigma_T}{m_e c^2} \sum_j T_{e,j} N_{e,j} \delta^{(2)}(\mathbf{r}_{\perp} - \mathbf{r}_{\perp,j}). \quad (14)$$

In the following step, we need to discretize the Compton- $y$  map into pixels. We can do this by averaging over pixel number  $k$  with area  $A_k$ :

$$y_k = \frac{1}{A_k} \int_{A_k} d\mathbf{r}_{\perp} y(\mathbf{r}_{\perp}). \quad (15)$$

Substituting Eq. (14) into the integral above gives counts of dark matter particles<sup>12</sup> in pixels weighted by their  $T_e N_e$  (determined via Eqs. (8) and (10)) along with constant factors:

$$y_k = \frac{1}{A_k} \frac{k_B \sigma_T}{m_e c^2} \sum_{j: r_{\perp,j} \in A_k} T_{e,j} N_{e,j}. \quad (16)$$

Subsequently, we need to convolve the pixelated map with the point spread function (the CMB instrument beam). We use fine pixels at this stage. The common beam for the ACT DR6 + *Planck* map has a Gaussian shape with 1.6 arcmin full width at half-maximum (Coulton et al. 2024). This translates to  $\approx 0.9h^{-1}\text{Mpc}$  at  $z = 0.8$  — close to the typical halo size. Thus, the exact width of the electron temperature-density profile is not so important.

Finally, we downsample the map to larger pixels, approximately matching the pixel side of 0.5 arcmin in the ACT DR6 + *Planck* Compton- $y$  map. Afterwards, we also apply a 2.4 arcmin FWHM Gaussian filter analogously to our data processing.

<sup>11</sup> Namely,  $\delta^{(3)}(\mathbf{r} - \mathbf{r}_j) = \delta^{(1)}(r_{\parallel} - r_{\parallel,j}) \delta^{(2)}(\mathbf{r}_{\perp} - \mathbf{r}_{\perp,j})$ . The integral of the former over  $dr_{\parallel}$  gives 1 as long as  $r_{\parallel,j}$  is not out of integration bounds.

<sup>12</sup> We use computational particles from a 3% subsample in Abacus belonging to each halo to track the dark matter mass structure. We initially put a mass of  $M_{\text{particle}}/0.03$  on each of these particles. Then, if the total mass put on particles in a halo is less than the mass of the halo, we put the remaining mass at the center of this halo (L2 according to Hadzhiyska et al. 2022). If the total mass put on particles in a halo exceed the mass of the halo, we downscale the masses on particles in this halo to match the halo mass, and do not add any mass at the center of the halo.

The naive expectation  $y \propto M_{\text{halo}}$  for the central Compton- $y$  parameter from a halo (using Eqs. (7), (8) and (11)) can hold for halos larger than the pixel, beam and filter size. For small, unresolved halos, there is an additional factor of halo area relative to the fixed pixel, beam or pixel area  $\propto R_{\text{halo}}^2 \propto M_{\text{halo}}^{2/3}$ . Alternatively, Eq. (16) can be used together with Eqs. (8) and (11) again. Either way, we obtain a steeper scaling  $y_{\text{map}} \propto M_{\text{halo}}^{5/3}$  as a simple expectation for smaller, unresolved halos.

Our simple tSZ model agrees with Yoshida et al. (2001) in the temperature estimate from dark matter velocity dispersion (Eq. (8)) and the ratio of electron number to dark matter mass (Eqs. (10) and (11), except our addition of the  $f_{\text{hot}}$  factor). In the following steps, we only track cluster structure via the computational dark matter particles, justifying this by the beam smearing, pixelation and further Gaussian filtering, whereas Yoshida et al. (2001) use more detailed density and velocity dispersion profiles. On the other hand, their model assumes isolated halos, whereas our treatment takes into account signal accumulation from multiple systems located close on the flat sky.

#### 4.2. Simple noise model

We generate noise maps as a Gaussian random field independent of the signal for simplicity. Signal and noise may be correlated in actual data processing (e.g., due to deprojection of different foregrounds), and this can account for some of the differences between data and mocks we notice later. On the other hand, we incorporate realistic spatial correlations and the varying pixel-wise Compton- $y$  standard deviation from the data. Without these, the mock clustering increases with tSZ SNR noticeably faster than in the data.

We take the power spectrum of the noise (normalized by the pixel-wise standard deviations  $\sigma_y$ ) from a filtered noise simulation provided with the ACT DR6 products (accordingly normalized, and filtered<sup>13</sup>). We generate a Gaussian random field in a periodic square grid (the same as for our Compton- $y$  signal map) from this power spectrum, subtract the mean and normalize by the standard deviation. We also create a periodic square map for the standard deviation  $\sigma_y$ , reproducing its distribution by area in the ACT DR6 + *Planck* noise maps restricted to the DESI sky footprint<sup>14</sup>. To obtain the total signal-to-noise ratio, we add the normalized noise to the ratio of the pure signal to the standard deviation, all taken from the pixel to which a mock galaxy falls.

This treatment allows us to mimic the zero-mean Gaussian fluctuations caused by instrumental noise and some component-separation systematics. However, it does not capture systematic biases, deviations from normal distribution and potential correlations between the signal and the noise. As a result, negative SNR in our mocks

<sup>13</sup> We applied our fiducial Gaussian filter after normalization by pixel-wise standard deviations (computed previously from 304 realizations of noise simulations). Filtering before normalization corresponds to the data processing more exactly, but it creates small-scale artifacts at the boundaries of regions observed by ACT to different depths.

<sup>14</sup> In our map,  $\sigma_y$  depends only on one coordinate, and increases symmetrically from the middle to the boundaries. This way, we respect the periodicity of the map inherited from the box.

only results from Gaussian smearing, whereas in data, systematic biases may also contribute.

### 4.3. Calibration

To refine our arbitrary coefficients in the  $y$  signal making described above, we rescale the signal to match the 3-dimensional density of  $> 4\sigma$  detections (cluster candidates) in the data ( $0.4 < z < 0.85$ ). This should be good as long as there is rarely more than one significant SZ cluster per pixel. Otherwise, we would need to match depth with the real Universe, which would be challenging with cut-sky mocks as well, because it would require bigger simulation boxes.

We match the ACT DR6 SZ cluster catalog (ACT/DES/HSC Collaboration et al. 2025) containing 9977 confirmed objects to the 6108 peaks ( $> 4\sigma$ ) detected within the cluster search area in the ACT DR6 + *Planck* tSZ Compton- $y$  map after our fiducial filtering. Because of the differences in the cluster candidate detection methods, the matching is not 1-to-1. We restrict good matches to 3523 unique clusters within 2.4 arcmin of our peaks, among which 1709 belong to our redshift range ( $0.4 < z < 0.85$ ). Given the sky area of the ACT DR6 cluster search mask, their average density is  $\approx 49(h^{-1}\text{Gpc})^{-3}$ . From this, we extrapolate the density of our  $> 4\sigma$  peaks as  $\approx 84(h^{-1}\text{Gpc})^{-3}$ . We rescale the mock  $y$  signal to match this density of  $> 4\sigma$  peaks in our first map (given that our simulation box is  $(2h^{-1}\text{Gpc})^3$ ). The resulting signal rescaling factor is  $\approx 1.05$ , which suggests that our rough assumptions in Section 4.1 were not far off, or their errors nearly compensated each other.

It is important to take noise into account in this calibration: without adding noise, we find the rescaling factor  $\approx 1.49$ . It can be expected because even though we use a normal (symmetric) distribution for noise, higher signals are rarer<sup>15</sup>. Therefore, at a given final signal-to-noise<sup>16</sup>, more objects were shifted “up” by noise (have a smaller true signal) than “down” (from a larger true signal).

### 4.4. Mock clustering

Bringing together all the ingredients, we can finally compare the clustering of SNR bins in mocks to data. We focus on the larger scales, showing cross-correlation function monopoles in Fig. 9 and relative galaxy bias in Fig. 10. We disregard the pairs with perpendicular separation  $r_p < 3.4 h^{-1}\text{Mpc}$ , which matches the angular separation cut we used for data (0.1 degrees) at  $z_{\text{mock}} = 0.8$ . The clustering/bias enhancement trend in mocks does not reproduce the data closely, although this should be expected from the simplicity of our modeling. The general similarity of the trend, however, suggests that our corresponding results for the data (Figs. 2 and 3) are not significantly driven by systematics (which are not included in our mocks).

One of the real data systematics not modeled in our cubic mocks is fiber assignment incompleteness (Bianchi et al. 2025). As this effect should lead to the under-representation of denser regions, we might expect lower

<sup>15</sup> That said, true negative signals are not possible in our simplistic model, and are probably hard to achieve in reality.

<sup>16</sup> At least a positive value.

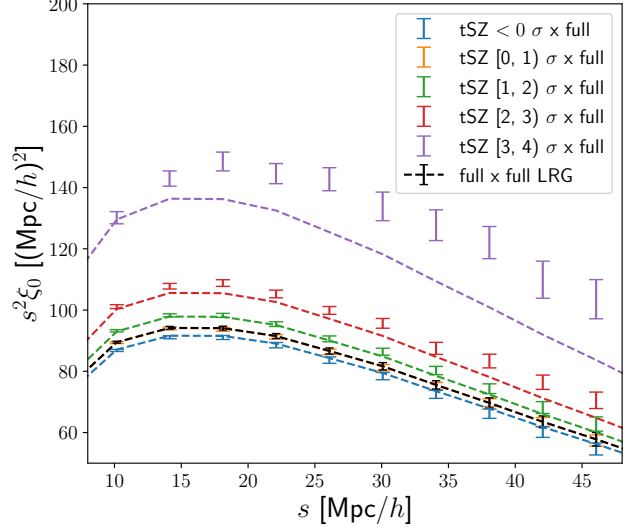


**Figure 9.** Mock large-scale isotropic (monopole) cross-correlation functions of different SNR bins with the full LRG sample (excluding pairs with perpendicular separation  $r_p < 3.4 h^{-1}\text{Mpc}$ ). Similarly to the data (Fig. 2), the clustering is enhanced at higher SNR, but less strongly. Also note that the  $[0, 1) \sigma$  bin remains very similar to the full sample. Colored dashed lines show the best fits obtained by scaling the full-sample autocorrelation function (black dashed line). The lines go below most of the points for higher-SNR bins, but keep in mind that strong correlations between the correlation function bins make fitting counterintuitive<sup>a</sup>. The scaling coefficients are the relative biases shown in Fig. 10.

<sup>a</sup>Detailed information about all fits is included in the supplementary material: doi:10.5281/zenodo.1694312

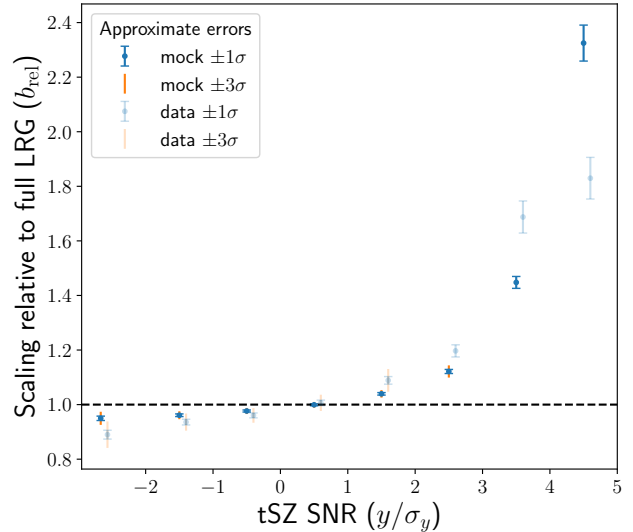


**Figure 10.** Mock galaxy bias of different SNR bins relative to the full LRG sample. Similarly to data (shaded and shifted slightly to the right for clarity), the relative bias increases with the SNR, but less rapidly near 0 and then more steeply at higher values.

relative bias for positive tSZ SNR in data compared to mocks. However, in Fig. 10, we see the opposite between 1 and  $4\sigma$ . This may be partially explained by the successful mitigation of fiber assignment incompleteness effects in large-scale clustering with weights (Bianchi et al. 2025; DESI Collaboration et al. 2025g) and on-sky separation ( $\theta$ ) cut (Pinon et al. 2025), as we use both on the data

side. Correcting for fiber assignment on small scales is a much more difficult problem, and this is a significant reason why we currently do not focus on the line-of-sight clustering (analogs of Figs. 5 and 6).

#### 4.5. Dependency on galaxy-halo connection

Our next step is to investigate how the different clustering in tSZ SNR bins reacts to changes in galaxy-halo connection assumptions. Doing this with all cross-correlation functions (Fig. 9) is hardly viable, because it would add even more lines to the plot, making it hard to interpret. The relative bias plot (Fig. 10) provides a cleaner way forward.

We use the 7-parameter halo occupation distribution (HOD) model (Zheng07+ $f_{\text{ic}} + \alpha_c + \alpha_s$ , but with  $f_{\text{ic}} = 1$ ) as in Yuan et al. (2024), implemented in ABACUSHOD (Yuan et al. 2022). 5 parameters describe the expected numbers of central and satellite galaxies in each halo (following Zheng et al. 2007):

$$\langle N_{\text{cen}}(M) \rangle = \frac{f_{\text{ic}}}{2} \left\{ 1 + \text{erf} \left[ \frac{\log(M/M_{\text{cut}})}{\sigma} \right] \right\}, \quad (17)$$

$$\langle N_{\text{sat}}(M) \rangle = \left[ \frac{\max(M - \kappa M_{\text{cut}}, 0)}{M_1} \right]^{\alpha} \langle N_{\text{cen}}(M) \rangle. \quad (18)$$

$M_{\text{cut}}$  sets the mass threshold for a halo to host a central galaxy.  $\sigma$  sets the rapidity of the transition from  $\approx 0$  to  $\approx 1$  central galaxies.  $M_1$  is a roughly typical mass for a halo hosting one satellite galaxy. Halos below the  $\kappa M_{\text{cut}}$  mass threshold will not have any satellite galaxies.  $\alpha$  is the power-law index for the number of satellite galaxies. Two remaining parameters describe the velocity bias:  $\alpha_c$  for centrals by scaling the Gaussian scatter  $\delta v(\sigma_{\text{LoS}})$  added to the halo center of mass velocity  $v_{\text{L2}}$ :

$$v_{\text{cen},z} = v_{\text{L2},z} + \alpha_c \delta v(\sigma_{\text{LoS}}), \quad (19)$$

and  $\alpha_s$  for satellites by shifting the galaxy's velocity from the velocity of a chosen dark matter computation particle  $v_{\text{p},z}$  towards the center of mass:

$$v_{\text{sat},z} = v_{\text{L2},z} + \alpha_s (v_{\text{p},z} - v_{\text{L2},z}). \quad (20)$$

Line-of-sight ( $z$ ) velocities are highlighted because we compute clustering in redshift space.

We vary each of the 7 HOD parameters by  $1\sigma$  up and down from the best fit, keeping the other parameters fixed. We take the best fits and the errorbars from the Zheng07+ $f_{\text{ic}} + \alpha_c + \alpha_s$  model analysis of LRG within  $0.6 < z < 0.8$  (Yuan et al. 2024) in the DESI Early Data Release. We only do not subsample for incompleteness, keeping  $f_{\text{ic}} = 1$ . We use 25 realizations (different phases in the initial conditions) of the base ABACUSUMMIT ( $2h^{-1}\text{Gpc}$ ) $^3$  box to obtain more robust mean shifts and estimate the sample covariance. For each realization, we make tSZ signal and noise maps<sup>17</sup>, save galaxy catalogs for the additional 14 HOD variants, split them into tSZ SNR bins according to the Compton- $y$  SNR map (the same across HOD variants for one realization), compute the clustering estimators and fit the relative scaling (bias).

<sup>17</sup> As described in Sections 4.1 and 4.2. We continue using the SNR rescaling calibrated on the first (ph000) realization in Section 4.3.

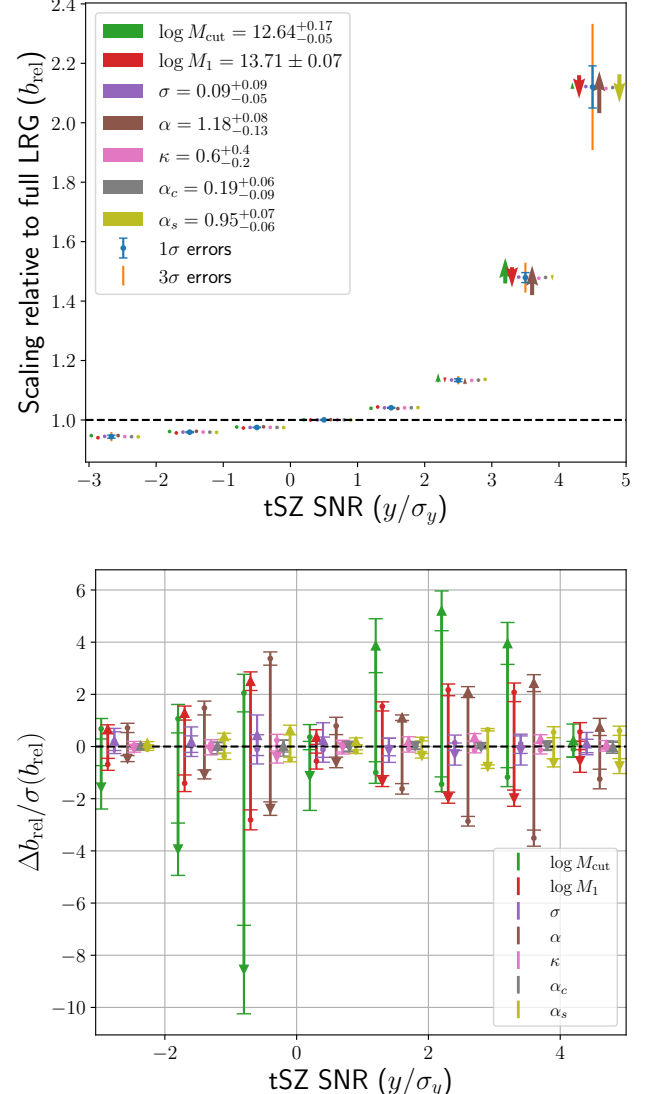


**Figure 11.** Effect of varying halo occupation distribution (HOD) parameters on clustering in different tSZ SNR bins. We shift each of the 7 parameters separately by  $1\sigma$  up and down from the best fit (following  $0.6 < z < 0.8$  LRG results from Yuan et al. 2024), keeping the other 6 parameters fixed. Logarithms are decimal, and masses are in  $h^{-1}M_{\odot}$ . Arrows are directed from a lower value of each parameter towards the higher one. Top panel: absolute changes in mock galaxy bias of different SNR bins relative to the full LRG sample, averaged over 25 realizations. Most changes are small and hard to see. Bottom panel: highlighted differences in each bin's relative bias with respect to the best-fit HOD, divided by the standard deviation estimate (for the  $(2h^{-1}\text{Gpc})^3$  box with full completeness). The ends of arrows represent averages over 25 realizations, the errorbars on them are for one realization (not for the mean, i.e., not divided by 5) and are estimated from the sample variance.

We keep the same tSZ map with varying HOD parameters, so the same halos remain in each SNR bin.  $M_{\text{cut}}$  and  $\sigma$  change the number of LRG centrals and satellites in these halos.  $M_1$ ,  $\alpha$  and  $\kappa$  only affect the number of satellites.  $\alpha_c$  and  $\alpha_s$  only alter redshift-space positions of centrals and satellites respectively. All these affect the redshift-space clustering of LRGs.

We show the changes in relative biases in each bin due to these HOD variations in the top panel of Fig. 11. Most

$(\Delta n_{\text{gal}})/n_{\text{gal}}$	$-1\sigma$	$+1\sigma$
$\log M_{\text{cut}} = 12.64_{-0.05}^{+0.17}$	13.2%	-34.8%
$\log M_1 = 13.71 \pm 0.07$	2.9%	-2.4%
$\sigma = 0.09_{-0.05}^{+0.09}$	-1.8%	7.1%
$\alpha = 1.18_{-0.13}^{+0.08}$	1.6%	-0.7%
$\kappa = 0.6_{-0.2}^{+0.4}$	1.2%	-2.2%
$\alpha_c = 0.19_{-0.09}^{+0.06}$	0	
$\alpha_s = 0.95_{-0.06}^{+0.07}$	0	

**Table 2**

Relative changes in mock number density with varying halo occupation distribution (HOD) parameters. We shift each of the 7 parameters separately by  $1\sigma$  up and down from the best fit (following  $0.6 < z < 0.8$  LRG results from [Yuan et al. 2024](#)), keeping the other 6 parameters fixed. Logarithms are decimal, and masses are in  $h^{-1} M_{\odot}$ . These values are averaged over 25 realizations. Note that we are keeping full completeness ( $f_{\text{ic}} = 1$  in [Eqs. \(17\)](#) and [\(18\)](#)). The velocity bias parameters  $\alpha_c$  and  $\alpha_s$  ([Eqs. \(19\)](#) and [\(20\)](#)) do not change the number density by construction.

of the differences are hard to discern (except some in the  $3 - 4$  and  $4 - 5$  SNR bins), but the errorbars are also hard to see in many of these cases. To address this issue, we take the differences between HOD variants and the best-fit HOD and divide by the errorbar estimate (for the best-fit HOD). The results are in the bottom panel of [Fig. 11](#).  $[0, 1] \sigma_y$  bin shows some of the least significant shifts, meaning that its bias relative to the full sample remains close to 1. Among the small differences for other bins, we can see larger effects of varying  $M_{\text{cut}}$ ,  $M_1$  and  $\alpha$ .

The relative bias shifts change sign between the  $[0, 1] \sigma$  bin and the  $[1, 2] \sigma$  bin for all parameters except  $\alpha_c$ <sup>18</sup> in the bottom panel of [Fig. 11](#). The direction flip in itself is only natural, because the average relative bias (weighted by the number<sup>19</sup> of galaxies in each corresponding SNR bin) should be 1<sup>20</sup>. However, it is not clear to us why the change of sign is around  $1\sigma$  tSZ detection significance specifically for most of the HOD parameters.

Despite several significant differences in the bottom panel of [Fig. 11](#), the relative bias pattern seems relatively insensitive to HOD. First, the variations due to  $M_{\text{cut}}$ ,  $M_1$  and  $\alpha$  are directed similarly and may be hard to disentangle. Second, the scale of HOD parameter variations is set by the precision of small-scale clustering in DESI Early Data Release (having a small volume but high completeness), whereas the errorbars of our relative biases are computed for a  $(2h^{-1}\text{Gpc})^3$  box (with full completeness). Third, we varied each parameter individually by its 1-dimensional standard deviation up and down instead of following the degeneracy directions. This should produce higher-significance differences in the full-sample clustering and number density. We show the relative changes in number density in [Table 2](#), and  $M_{\text{cut}}$  variations have the largest effect (however, note that we are keeping full completeness,  $f_{\text{ic}} = 1$  in [Eqs. \(17\)](#) and [\(18\)](#)). The stability of the relative bias pattern with HOD would

<sup>18</sup> For  $\alpha_c$ , the sign flips between  $[-1, 0] \sigma$  and  $[0, 1] \sigma$ , but all the differences have very low significance.

<sup>19</sup> For data, it should be weighted by the sum of clustering weights. But in our cubic mocks, all the galaxies have weights set to 1.

<sup>20</sup> As it is defined as the scaling of the full-sample auto-correlation function to best match the SNR bin-full sample cross-correlation functions

be beneficial for the precision and robustness of cosmological inference from tSZ-split clustering, and we will validate this preliminary finding further in future work.

#### 4.6. Relating halo mass to thermal Sunyaev-Zeldovich observables

Simulations also allow us to access the true halo properties, unlike the data. With this, we can explore connections with SZ properties (bearing in mind they are produced approximately).

We present correlations between host halo mass and several tSZ quantities for mock galaxies<sup>21</sup> in [Fig. 12](#). We count LRGs from a single mock galaxy catalog created with the fiducial HOD model, having their host halo mass listed in the mock catalog<sup>22</sup>, and obtain tSZ quantities by matching them to our map pixels. In the upper panel of [Fig. 12](#) we see a power-law relation between the halo mass and the unfiltered noiseless Compton- $y$ . The power-law looks slightly steeper than  $y \propto M_{\text{halo}}$  (estimated with big simplifications in [Section 4.1](#); the index may be similar to  $\approx 1.08$  from Eq. (4) in [ACT/DES/HSC Collaboration et al. 2025](#)). The trend smears up for smaller halo masses; this may be caused by such halos appearing close (within the point spread function) to slightly larger halos. The middle panel of [Fig. 12](#) shows a range of SNR values centered on zero for lower halo masses (as expected from Gaussian noise and negligible signal) and a noticeable increase for larger halo masses.

In the bottom panel of [Fig. 12](#), we explore the realistic observables in more detail by first splitting the data into SNR bins and then producing 1D histograms of halo mass in each. The lower-SNR bins ( $y/\sigma_y < 4$ ) are dominated by galaxies from  $M_{\text{halo}} \approx 10^{12.7} M_{\odot}$  halos, but the distributions have a long higher-mass tail, and it extends further and further with increasing SNR. In the  $[3, 4] \sigma_y$  bin, a secondary bump at the high mass ends becomes visible, and it dominates in the higher ( $y/\sigma_y \geq 4$ ) bins. Thus, a qualitative transition occurs between 3 and  $4 \sigma_y$ .

We also repeat the binning in the signal (Compton- $y$  parameter not divided by  $\sigma_y$ ). We have chosen the bin width as the mean  $\sigma_y$  across the map for easier comparison with the SNR binning. The two resulting distributions in the bottom panel of [Fig. 12](#) are very similar (differences are visible only in the higher-SNR bins), reinforcing our arguments from [Section 3.1](#).

A well-known or calibrated relation between the galaxy host halo masses and tSZ observables can be used to make theoretical predictions about tSZ-split galaxy clustering, especially on larger scales. Furthermore, if this relation is less dependent on cosmology than halo mass-density relations, it would enable more robust cosmolog-

<sup>21</sup> We include these properties for all galaxies in the supplementary material, doi:10.5281/zenodo.16943122, and encourage searching for other interesting relations.

<sup>22</sup> Therefore, the absence of  $M_{\text{halo}} \lesssim 10^{12.3} M_{\odot}/h$  is not a limitation of halos in the ABACUSUMMIT simulation but a reflection of the best-fit HOD model from [Yuan et al. \(2024\)](#). We tried plotting halo mass distributions, but found it much less informative due to a very strong contribution of smaller halos down to  $\sim 10^{11} M_{\odot}/h$  that would almost never host LRGs. The absence of  $M_{\text{halo}} \lesssim 10^{11} M_{\odot}/h$  halos in ABACUSUMMIT "base" boxes we used might lead to misestimation of the mock tSZ signal, but their contribution is likely not very significant (as we naively expect  $y_{\text{map}} \propto M_{\text{halo}}^{5/3}$  for each very low-mass halo from [Section 4.1](#), and the more realistic power index may be even steeper).

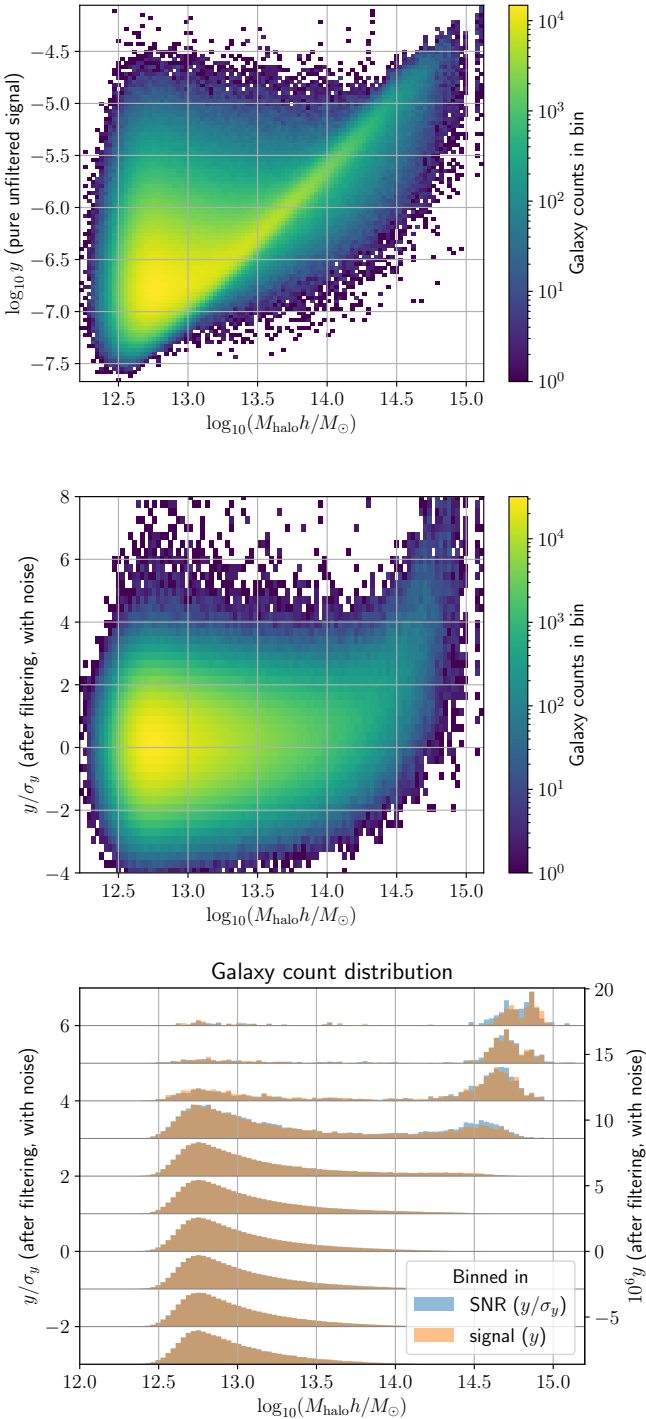


**Figure 12.** Histograms displaying correlations between LRG host halo masses and tSZ quantities in the corresponding pixels in our mock map (assuming ACT DR6 + *Planck* characteristics following [Coulton et al. 2024](#); [Atkins et al. 2023](#)). Top: 2D histogram using the noiseless  $y$  parameter without filtering. Middle: 2D histogram using the tSZ SNR with our fiducial filter and simplistic noise. Bottom: 1D histograms of halo mass in SNR (blue) or signal (orange) bins (the two distributions are very similar; both observables include our fiducial filter and simplistic noise). All histograms are weighted by galaxy counts from one mock catalog with the fiducial HOD model (see [Section 4.5](#)).

ical inference beyond the 2-point function. A theoretical or semi-analytical model would be a very attractive alternative to a simulation-based model (like for density-split clustering in [Cuesta-Lazaro et al. 2024](#)) requiring a large number of high-quality mocks.

## 5. CONCLUSIONS

We propose to split the spectroscopic galaxy samples into distinct subpopulations by the signal-to-noise ratio for the thermal Sunyaev-Zeldovich effect. This effect has long been associated with galaxy clusters ([Sunyaev & Zeldovich 1970](#)) and is an established tool for their detection and property determination ([Planck Collaboration et al. 2016b](#); [Hilton et al. 2021](#); [Robertson et al. 2024](#); [Bocquet et al. 2024](#); [Kornoelje et al. 2025](#); [ACT/DES/HSC Collaboration et al. 2025](#)). However, the rigorously detected clusters ( $> 4\sigma$  in [Hilton et al. 2021](#); [ACT/DES/HSC Collaboration et al. 2025](#)) are relatively uncommon. We focus on the larger areas of the map with lower signal-to-noise, and demonstrate that they can enable us to extract more valuable cosmological information from galaxy clustering.

From large-scale clustering ([Fig. 2](#)), we find that a higher tSZ signal-to-noise ratio corresponds to galaxies with a higher bias ([Fig. 3](#)). We see a similar increase in clustering amplitude in the projected correlation function ([Fig. 4](#)), which can be used with larger photometric galaxy samples (e.g., [Zhou et al. 2023b](#)). The clustering enhancement with tSZ can allow us to select luminous red galaxy sub-samples and test the consistency of large-scale patterns in them (e.g., following [Patej & Eisenstein 2016](#)), or better understand their biases to obtain tighter constraints on primordial non-Gaussianity (in the spirit of [Sullivan et al. 2023](#)).

From small-scale line-of-sight clustering, we find that the velocity dispersion increases considerably with tSZ SNR ([Fig. 6](#)). This is likely a clean indication of strong non-perturbative non-linearities (Fingers of God) which can be removed to improve the theoretical modeling ([Baleato Lizancos et al. 2025](#)). We further show how the velocity dispersion is reduced by putting an upper threshold on the tSZ SNR ([Fig. 7](#)).

We also see that galaxies with higher tSZ SNR have higher numbers of close neighbors ([Fig. 8](#)). We remind the reader that the number of close on-sky neighbors in DESI data is suppressed by fiber collisions ([DESI Collaboration et al. 2025g](#); [Bianchi et al. 2025](#)). As an external indicator, tSZ could help inform the galaxy multiplet studies using spectroscopic (e.g., [Lamman et al. 2024](#)) or photometric data.

We have built a simple mock tSZ map that allowed us to reproduce general trends from the data ([Figs. 9 and 10](#)). However, we note differences, and investigating their causes will be our next priority. We also tentatively investigate how the galaxy-halo connection (halo occupation distribution) affects the relative bias of different tSZ bins ([Fig. 11](#)) and find relatively small changes.

In further work, we aim to develop cosmological inference from tSZ-split clustering (e.g., constraining the cosmic growth of structure). One avenue is to build a simulation-based model or inference pipeline, like for density-split ([Cuesta-Lazaro et al. 2024](#)) or density-marked clustering ([Massara et al. 2024](#)). However, this requires investing in a large number of accurate simula-

tions with different cosmological and galaxy-halo connection parameters. We have presented preliminary simulation-based results on the halo mass-tSZ observables relation in Fig. 12, which look sensible and consistent with previous works. Together with hints of weak sensitivity to the galaxy-halo connection, this gives us hope of building a semi-analytical model by calibrating the relation between the halo mass and the thermal Sunyaev-Zeldovich observables using relatively few simulations.

tSZ splitting could be useful beyond luminous red galaxies, although it might be less efficient. At higher redshifts, there are fewer SZ clusters (ACT/DES/HSC Collaboration et al. 2025), and the density of galaxies is lower, meaning that splitting would be more harmful for the signal-to-noise ratio of the measurements. At lower redshifts (like DESI Bright Galaxy Sample/Survey, Hahn et al. 2023), X-ray observations may be a cleaner indicator of clusters, and the higher density allows for a better direct detection of close multiplets in spectroscopic data.

Combining 3D galaxy surveys and Sunyaev-Zeldovich data is very promising. As well as the number of spectra with DESI, the SZ measurements are improving rapidly with the current and next CMB experiments like Simons Observatory (SO, Ade et al. 2019) and CMB-S4 (Abazajian et al. 2019; Carlstrom et al. 2019). The overlap of the SO large-aperture telescope (LAT) survey with DESI is similar to ACT DR6, but the combined depth is expected to improve from  $10 \mu\text{K-arcmin}$  in ACT DR6 (Coulton et al. 2024) to  $6 \mu\text{K-arcmin}$  for the baseline SO LAT (Ade et al. 2019) and  $2.4 \mu\text{K-arcmin}$  for the enhanced SO LAT expected to be complete by 2028 (The Simons Observatory Collaboration et al. 2025). There are also possibilities to use larger photometric samples further in celestial South from DESI Legacy Imaging surveys (e.g., extended LRG sample Zhou et al. 2023b) and LSST (Ivezić et al. 2019) in the future with projected statistics or using photometric redshifts. Joint analysis of different measurements has high potential to improve our measurements and uncover new tensions.

#### ACKNOWLEDGMENTS

We thank Antón Baleato Lizancos and Ravi K. Sheth for their very fruitful feedback and suggestions. MR and DJE have been supported by U.S. Department of Energy grant DE-SC0013718 and by the Simons Foundation Investigator program.

This material is based upon work supported by the U.S. Department of Energy (DOE), Office of Science, Office of High-Energy Physics, under Contract No. DE-AC02-05CH11231, and by the National Energy Research Scientific Computing Center, a DOE Office of Science User Facility under the same contract. Additional support for DESI was provided by the U.S. National Science Foundation (NSF), Division of Astronomical Sciences under Contract No. AST-0950945 to the NSF’s National Optical-Infrared Astronomy Research Laboratory; the Science and Technology Facilities Council of the United Kingdom; the Gordon and Betty Moore Foundation; the Heising-Simons Foundation; the French Alternative Energies and Atomic Energy Commission (CEA); the National Council of Humanities, Science and Technology of Mexico (CONAH-CYT); the Ministry of Science, Innovation and Universi-

ties of Spain (MICIU/AEI/10.13039/501100011033), and by the DESI Member Institutions: <https://www.desi.lbl.gov/collaborating-institutions>. Any opinions, findings, and conclusions or recommendations expressed in this material are those of the author(s) and do not necessarily reflect the views of the U. S. National Science Foundation, the U. S. Department of Energy, or any of the listed funding agencies.

The authors are honored to be permitted to conduct scientific research on I’oligam Du’ag (Kitt Peak), a mountain with particular significance to the Tohono O’odham Nation.

This work has used the following software packages: ASTROPY (Astropy Collaboration et al. 2013, 2018, 2022), HEALPY and HEALPIX<sup>23</sup> (Zonca et al. 2019; Górski et al. 2005; Zonca et al. 2023), JUPYTER (Perez & Granger 2007; Kluyver et al. 2016), MATPLOTLIB (Hunter 2007), NUMPY (Harris et al. 2020), PIXELL<sup>24</sup>, PYCORR<sup>25</sup> (de Mattia et al. 2024; Sinha & Garrison 2020, 2019), PYTHON (Van Rossum & Drake 2009), SCIPY (Virtanen et al. 2020; Gommers et al. 2023), and SCIKIT-LEARN (Pedregosa et al. 2011; Buitinck et al. 2013; Grisel et al. 2023).

This research has used NASA’s Astrophysics Data System. Software citation information has been aggregated using The Software Citation Station (Wagg & Broekgaarden 2024; Wagg et al. 2024).

#### DATA AVAILABILITY

DESI Data Release 1 is available at <https://data.desi.lbl.gov/doc/releases/dr1/>; the clustering catalogs used in this work can be found at <https://data.desi.lbl.gov/public/dr1/survey/catalogs/dr1/LSS/iron/LSScats/v1.5/>. ACT Data Release 6 maps and noise simulations used in this work are available at [https://portal.nersc.gov/project/act/dr6\\_nilc/](https://portal.nersc.gov/project/act/dr6_nilc/). All the points from the figures, together with some additional data and the source code, are available at doi:10.5281/zenodo.1694312.

#### REFERENCES

- ACT/DES/HSC Collaboration et al., 2025, arXiv e-prints, p. arXiv:2507.21459
- Abazajian K., et al., 2019, arXiv e-prints, p. arXiv:1907.04473
- Ade P., et al., 2019, *J. Cosmology Astropart. Phys.*, 2019, 056
- Astropy Collaboration et al., 2013, *A&A*, 558, A33
- Astropy Collaboration et al., 2018, *AJ*, 156, 123
- Astropy Collaboration et al., 2022, *ApJ*, 935, 167
- Atkins Z., et al., 2023, *J. Cosmology Astropart. Phys.*, 2023, 073
- Aviles A., Koyama K., Cervantes-Cota J. L., Winther H. A., Li B., 2020, *J. Cosmology Astropart. Phys.*, 2020, 006
- Baleato Lizancos A., Seljak U., Karamanis M., Bonici M., Ferraro S., 2025, *J. Cosmology Astropart. Phys.*, 2025, 014
- Bermejo-Climent J. R., et al., 2025, *A&A*, 698, A177
- Bianchi D., et al., 2025, *J. Cosmology Astropart. Phys.*, 2025, 074
- Bocquet S., et al., 2024, *Phys. Rev. D*, 110, 083509
- Buitinck L., et al., 2013, in ECML PKDD Workshop: Languages for Data Mining and Machine Learning. pp 108–122
- Carlstrom J., et al., 2019, in Bulletin of the American Astronomical Society. p. 209 (arXiv:1908.01062)
- Chaussidon E., et al., 2025, arXiv e-prints, p. arXiv:2503.24343
- Chen S.-F., Zaldarriaga M., 2025, arXiv e-prints, p. arXiv:2505.00659

<sup>23</sup> <https://healpix.sourceforge.net>

<sup>24</sup> <https://github.com/simonsobs/pixell>

<sup>25</sup> <https://github.com/cosmodesi/pycorr>

Chen S.-F., Howlett C., Lai Y., Qin F., 2025, arXiv e-prints, p. arXiv:2508.00066

Choi S. K., et al., 2020, *J. Cosmology Astropart. Phys.*, 2020, 045

Coulton W., et al., 2024, *Phys. Rev. D*, 109, 063530

Cuesta-Lazaro C., et al., 2024, *MNRAS*, 531, 3336

DESI Collaboration 2026, in preparation

DESI Collaboration et al., 2016a, arXiv e-prints, p. arXiv:1611.00036

DESI Collaboration et al., 2016b, arXiv e-prints, p. arXiv:1611.00037

DESI Collaboration et al., 2022, *AJ*, 164, 207

DESI Collaboration et al., 2024a, arXiv e-prints, p. arXiv:2411.12021

DESI Collaboration et al., 2024b, *AJ*, 167, 62

DESI Collaboration et al., 2024c, *AJ*, 168, 58

DESI Collaboration et al., 2025a, arXiv e-prints, p. arXiv:2503.14738

DESI Collaboration et al., 2025b, arXiv e-prints, p. arXiv:2503.14739

DESI Collaboration et al., 2025c, arXiv e-prints, p. arXiv:2503.14745

DESI Collaboration et al., 2025d, *J. Cosmology Astropart. Phys.*, 2025, 124

DESI Collaboration et al., 2025e, *J. Cosmology Astropart. Phys.*, 2025, 021

DESI Collaboration et al., 2025f, *J. Cosmology Astropart. Phys.*, 2025, 012

DESI Collaboration et al., 2025g, *J. Cosmology Astropart. Phys.*, 2025, 017

DESI Collaboration et al., 2025h, *J. Cosmology Astropart. Phys.*, 2025, 028

Davis M., Peebles P. J. E., 1983, *ApJ*, 267, 465

Diaferio A., Sunyaev R. A., Nusser A., 2000, *ApJL*, 533, L71

Ebina H., White M., 2025, *J. Cosmology Astropart. Phys.*, 2025, 150

Farren G. S., et al., 2024, *ApJ*, 966, 157

Ferraro S., Sailer N., Slosar A., White M., 2022, arXiv e-prints, p. arXiv:2203.07506

Fowler J. W., et al., 2007, *Appl. Opt.*, 46, 3444

Fukugita M., Hogan C. J., Peebles P. J. E., 1998, *ApJ*, 503, 518

Garrison L. H., Eisenstein D. J., Ferrer D., Maksimova N. A., Pinto P. A., 2021, *MNRAS*, 508, 575

Gommers R., et al., 2023, *scipy/scipy: SciPy 1.11.4*, doi:10.5281/zenodo.10155614, <https://doi.org/10.5281/zenodo.10155614>

Górski K. M., Hivon E., Banday A. J., Wandelt B. D., Hansen F. K., Reinecke M., Bartelmann M., 2005, *ApJ*, 622, 759

Grisel O., et al., 2023, *scikit-learn/scikit-learn: Scikit-learn 1.3.2*, doi:10.5281/zenodo.10034229, <https://doi.org/10.5281/zenodo.10034229>

Guy J., et al., 2023, *AJ*, 165, 144

Hadzhiyska B., Eisenstein D., Bose S., Garrison L. H., Maksimova N., 2022, *MNRAS*, 509, 501

Hahn C., et al., 2023, *AJ*, 165, 253

Harris C. R., et al., 2020, *Nature*, 585, 357

Hilton M., et al., 2021, *ApJS*, 253, 3

Hunter J. D., 2007, *Computing in Science & Engineering*, 9, 90

Ivezić Ž., et al., 2019, *ApJ*, 873, 111

Kaiser N., 1987, *MNRAS*, 227, 1

Kim J., et al., 2024, *J. Cosmology Astropart. Phys.*, 2024, 022

Kluyver T., et al., 2016, in Loizides F., Schmidt B., eds, *Positioning and Power in Academic Publishing: Players, Agents and Agendas*. pp 87 – 90

Kornoelje K., et al., 2025, arXiv e-prints, p. arXiv:2503.17271

Krolewski A., et al., 2024, *J. Cosmology Astropart. Phys.*, 2024, 021

Lamman C., et al., 2024, *MNRAS*, 534, 3540

Landy S. D., Szalay A. S., 1993, *ApJ*, 412, 64

Levi M., et al., 2013, arXiv e-prints, p. arXiv:1308.0847

Liu R. H., et al., 2025a, arXiv e-prints, p. arXiv:2502.08850

Liu R. H., Hadzhiyska B., Ferraro S., Bose S., Hernández-Aguayo C., 2025b, arXiv e-prints, p. arXiv:2504.11794

Maksimova N. A., Garrison L. H., Eisenstein D. J., Hadzhiyska B., Bose S., Satterthwaite T. P., 2021, *MNRAS*, 508, 4017

Massara E., Villaescusa-Navarro F., Ho S., Dalal N., Spergel D. N., 2021, *Phys. Rev. Lett.*, 126, 011301

Massara E., et al., 2023, *ApJ*, 951, 70

Massara E., et al., 2024, arXiv e-prints, p. arXiv:2404.04228

Maus M., et al., 2025, arXiv e-prints, p. arXiv:2505.20656

Morawetz J., Paillas E., Percival W. J., 2025, *J. Cosmology Astropart. Phys.*, 2025, 026

Osato K., Nagai D., 2023, *MNRAS*, 519, 2069

Paillas E., Cai Y.-C., Padilla N., Sánchez A. G., 2021, *MNRAS*, 505, 5731

Paillas E., et al., 2023, *MNRAS*, 522, 606

Paillas E., et al., 2024, *MNRAS*, 531, 898

Patej A., Eisenstein D., 2016, *MNRAS*, 460, 1310

Pedregosa F., et al., 2011, *Journal of Machine Learning Research*, 12, 2825

Peebles P. J. E., 1976, *Ap&SS*, 45, 3

Perez F., Granger B. E., 2007, *Computing in Science and Engineering*, 9, 21

Philcox O. H. E., Massara E., Spergel D. N., 2020, *Phys. Rev. D*, 102, 043516

Philcox O. H. E., Aviles A., Massara E., 2021, *J. Cosmology Astropart. Phys.*, 2021, 038

Pinon M., et al., 2025, *J. Cosmology Astropart. Phys.*, 2025, 131

Planck Collaboration et al., 2016a, *A&A*, 594, A22

Planck Collaboration et al., 2016b, *A&A*, 594, A27

Planck Collaboration et al., 2020a, *A&A*, 641, A1

Planck Collaboration et al., 2020b, *A&A*, 641, A6

Poppett C., et al., 2024, *AJ*, 168, 245

Robertson N. C., et al., 2024, *A&A*, 681, A87

Sailer N., et al., 2025, *J. Cosmology Astropart. Phys.*, 2025, 008

Schlafly E. F., et al., 2023, *AJ*, 166, 259

Schlegel D. J., et al., 2022, arXiv e-prints, p. arXiv:2209.03585

Sheth R. K., 1996, *MNRAS*, 279, 1310

Silber J. H., et al., 2023, *AJ*, 165, 9

Sinha M., Garrison L. H., 2019, in *Software Challenges to Exascale Computing. Second Workshop*. pp 3–20 (arXiv:1911.08275), doi:10.1007/978-981-13-7729-7\_1

Sinha M., Garrison L. H., 2020, *MNRAS*, 491, 3022

Stein G., Alvarez M. A., Bond J. R., van Engelen A., Battaglia N., 2020, *J. Cosmology Astropart. Phys.*, 2020, 012

Sullivan J. M., Prijon T., Seljak U., 2023, *J. Cosmology Astropart. Phys.*, 2023, 004

Sunyaev R. A., Zeldovich Y. B., 1970, *Ap&SS*, 7, 3

Sunyaev R. A., Zeldovich Y. B., 1972, *Comments on Astrophysics and Space Physics*, 4, 173

Sunyaev R. A., Zeldovich I. B., 1980, *ARA&A*, 18, 537

The Simons Observatory Collaboration et al., 2025, *J. Cosmology Astropart. Phys.*, 2025, 034

Turin G., 1960, *IRE Transactions on Information Theory*, 6, 311

Van Rossum G., Drake F. L., 2009, *Python 3 Reference Manual*. CreateSpace, Scotts Valley, CA

Virtanen P., et al., 2020, *Nature Methods*, 17, 261

Wagg T., Broekgaarden F. S., 2024, arXiv e-prints, p. arXiv:2406.04405

Wagg T., Broekgaarden F., Gültekin K., 2024, *TomWagg/software-citation-station: v1.2*, doi:10.5281/zenodo.13225824, <https://doi.org/10.5281/zenodo.13225824>

White M., 2016, *J. Cosmology Astropart. Phys.*, 2016, 057

Yoshida N., Sheth R. K., Diaferio A., 2001, *MNRAS*, 328, 669

Yuan S., Garrison L. H., Hadzhiyska B., Bose S., Eisenstein D. J., 2022, *MNRAS*, 510, 3301

Yuan S., et al., 2024, *MNRAS*, 530, 947

Zheng Z., Coil A. L., Zehavi I., 2007, *ApJ*, 667, 760

Zhou R., et al., 2023a, *AJ*, 165, 58

Zhou R., et al., 2023b, *J. Cosmology Astropart. Phys.*, 2023, 097

Zonca A., Singer L., Lenz D., Reinecke M., Rosset C., Hivon E., Gorski K., 2019, *Journal of Open Source Software*, 4, 1298

Zonca A., et al., 2023, *healpy/healpy: 1.16.6*, doi:10.5281/zenodo.8404216, <https://doi.org/10.5281/zenodo.8404216>

de Mattia A., Rashkovetskyi M., Sinha M., Garrison L. H., 2024, *pycorr: Two-point correlation function estimation*, Astrophysics Source Code Library, record ascl:2403.009

provides fast and easy peer review for new papers in the **astro-ph** section of the arXiv, making the reviewing pro-

cess simpler for authors and referees alike. Learn more at <http://astro.theoj.org>.